


Article

A Comparative Study of Differential Quadrature Methods for METE Nanobeam Vibrations

Waleed Mohammed Abdelfattah 

College of Engineering, University of Business and Technology, Jeddah 23435, Saudi Arabia;
w.abdelfattah@ubt.edu.sa

Abstract: This study investigates the use of three different quadrature schemes, as well as an iterative quadrature methodology, to analyze vibrations in magneto-electro-thermo-elastic nanobeams. Individual MATLAB programs for each method are developed with the goal of minimizing errors in comparison to accurate findings, as well as determining the execution time for each strategy. This study shows that the Discrete Singular-Convolution Differential Quadrature Method with a Regularized Shannon Kernel (DSCDQM-RSK) and specified parameters produces the best accurate and efficient results for this particular situation. A subsequent parametric study is carried out to determine the effect of various factors on the vibrated nanobeam, including boundary conditions, material types, linear and nonlinear elastic foundation properties, nonlocal parameters, length-to-thickness ratios, external electric and magnetic potentials, axial forces, and temperature variations. Important discoveries include insights into the relationship between fundamental frequency, linear elastic foundation features, axial loads, external magnetic fields, temperature fluctuations, and material types. According to this study, these findings could be critical in the development of sophisticated nanostructures made from magneto-electro-thermo-elastic materials for use in a variety of electromechanical applications. This would entail utilizing nanobeams' unique properties in applications such as sensors, resonators, and transducers for nanoelectronics and biology.

Keywords: piezomagnetic composites; nonlocal elasticity; Timoshenko beam theory; vibration analysis; nonlinear foundations; PDQM



Academic Editor: Binlin Zhang

Received: 12 December 2024

Revised: 13 January 2025

Accepted: 23 January 2025

Published: 25 January 2025

Citation: Abdelfattah, W.M. A Comparative Study of Differential Quadrature Methods for METE Nanobeam Vibrations. *Algorithms* **2025**, *18*, 64. <https://doi.org/10.3390/a18020064>

Copyright: © 2025 by the author. Licensee MDPI, Basel, Switzerland. This article is an open access article distributed under the terms and conditions of the Creative Commons Attribution (CC BY) license (<https://creativecommons.org/licenses/by/4.0/>).

1. Introduction

Magneto-electro-thermo-elastic (METE) composites, comprising piezoelectric and piezomagnetic phases, exhibit remarkable energy conversion capabilities, transforming electric, thermal, elastic, and magnetic energy [1,2]. Their versatility has led to widespread adoption in various fields, including vibration control, actuation, sensing, medical devices, health monitoring systems, and energy harvesting [3,4].

This section analyzes the available literature on the analysis of magneto-electro-elastic systems. Wu et al. [5] investigated the static behavior of 3D, doubly curved, functionally graded magneto-electro-elastic shells under combined mechanical, electrical, and magnetic loads. Huang et al. [6] proposed analytical and semi-analytical solutions for anisotropic, functionally graded magneto-electro-elastic beams under arbitrary stresses, based on sinusoidal series expansions. Chang [7] investigated the vibration characteristics of transversely isotropic magneto-electro-elastic rectangular plates, considering various vibration conditions (free, deterministic, and random) within fluid environments. Ansari et al. [8] developed a nonlocal, geometrically nonlinear beam model for magneto-electro-thermo-elastic

nanobeams subjected to external electric voltage, magnetic potential, and temperature changes. Finally, Ke et al. [9] analyzed the free vibration of embedded magneto-electro-elastic cylindrical nanoshells using Love's shell theory. These studies collectively provide a foundation for understanding the diverse mechanical and vibrational behaviors of magneto-electro-elastic materials across different structural configurations.

Prior research has examined the response of magneto-electro-elastic materials under various loading conditions. Wu et al. [5] investigated the static behavior of three-dimensional (3D), doubly curved, functionally graded magneto-electro-elastic shells subjected to combined mechanical, electrical, and magnetic loads. Huang et al. [6] developed analytical and semi-analytical solutions for anisotropic, functionally graded magneto-electro-elastic beams under arbitrary loading. These studies provide a foundation for understanding the complex interactions between mechanical, electrical, and magnetic fields within these materials. Chang [7] studied the vibration characteristics of transversely isotropic magneto-electro-elastic rectangular plates, considering free, deterministic, and random vibrations in fluid environments. Furthermore, studies have explored the behavior of magneto-electro-elastic nanostructures. Ansari et al. [8] developed a nonlocal, geometrically nonlinear beam model to analyze the behavior of magneto-electro-thermo-elastic nanobeams under various external stimuli. Ke et al. [9] investigated the free vibration properties of embedded magneto-electro-elastic cylindrical nanoshells, considering size-dependent effects.

The field has seen substantial growth, particularly in the investigation of magneto-electro-thermo-elastic (METE) nanomaterials and nanostructures. Studies have focused on materials such as BiFeO₃, BiTiO₃-CoFe₂O₄, NiFe₂O₄-PZT, and various nanowire and nanobeam configurations [10,11]. The recent incorporation of PTZ-5H-COFe₂O₄ further expands the potential applications of these materials.

The investigation of nanoscale phenomena frequently employs nonlocal elasticity theory [12,13]. While experimental characterization at the nanoscale level presents significant challenges, and molecular dynamics simulations incur high computational costs, continuum models remain crucial for nanostructure research [14–16]. However, compelling evidence suggests that the nonlocal effect, arising from the inherent small-length scales, significantly influences the mechanical properties of nanostructures [15–17]. This necessitates the incorporation of nonlocal considerations into traditional structural theories to accurately capture the size-dependent behavior observed in these systems [18].

Numerous recent publications have focused on exploring the static and dynamic characteristics of magneto-electro-thermo-Elastic (METE) nanobeams. These works introduce exact and semi-analytical techniques for addressing linear free and forced vibrations, as well as buckling phenomena in nanobeams [19–21]. Additionally, alternative numerical approaches such as finite element analysis [22], meshless methods [23], higher-order B-spline finite strip modeling [24], and Rayleigh-Ritz methods [25] have been investigated for tackling these issues. However, all these methodologies demand a significant number of grid points and substantial computational resources to achieve a satisfactory level of precision.

The Polynomial-Based Differential Quadrature Method (PDQM) has been proven to be able to produce correct results with fewer grid points [26–30], in contrast to many numerical methods [31–33]. More reliable substitutes are provided by the Discrete Singular-Convolution Differential Quadrature Method (DSCDQM) [34] and the Sinc Differential Quadrature Method (SDQM) [35]. The selection of shape functions, such as the Regularized Shannon Kernel (RSK), Delta Lagrange Kernel (DLK), and cardinal sine function, which enhance solution convergence and stability, is crucial to the efficacy of these techniques [36–40].

Using the Sinc Differential Quadrature Method (SDQM) and Discrete Singular-Convolution Differential Quadrature Method (DSCDQM), this study examines the vibration properties of magneto-electro-thermo-elastic (METE) nanobeams sitting on nonlinear elastic substrates. Although there are several numerical methods [31–33], the PDQM has been proven to be able to provide precise results using fewer grid points [26–30]. Better accuracy and stability are provided by the SDQM [35] and DSCDQM [34] than by the conventional Polynomial-Based DQM. To improve the convergence and stability of the numerical solutions, these techniques rely on the selection of suitable shape functions, such as the Regularized Shannon Kernel (RSK), Delta Lagrange Kernel (DLK), and cardinal sine function [36–40]. By creating innovative numerical algorithms and comparing them to proven analytical and numerical results, this study pioneers the application of the SDQM and DSCDQM to this particular situation.

The impact of various parameters on the natural frequencies and mode shapes of the METE nanobeams are analyzed through a thorough parametric investigation. Axial loads, external magnetic potentials, temperature fluctuations, boundary conditions, material qualities, nonlocal parameters, axial loads, nonlinear and linear elastic foundations, and aspect ratios are some of these variables. The structure of this paper is as follows: the mathematical formulation is explained in depth in Section 2, the numerical methods are described in Section 3, the results and discussion are presented in Sections 4 and 5, and the main conclusions and future research areas are discussed in Section 6.

2. Formulation of the Problem

Consider a METE nanobeam of dimensions $L \times h$ subjected to various external stimuli. The beam is exposed to an electric voltage, $\phi(x, z, t)$, a magnetic potential, $\psi(x, z, t)$, a temperature change, ΔT , and a mechanical potential, P_0 . Moreover, the beam is supported by a nonlinear elastic foundation, which is defined by the stiffness coefficients K_1 , K_2 , and K_3 , representing linear and nonlinear characteristics, respectively, as depicted in Figure 1.

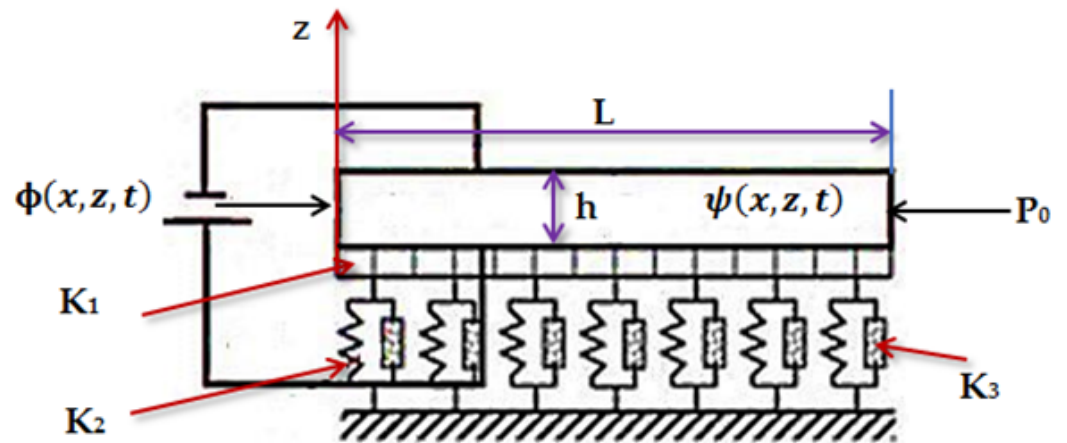


Figure 1. Schematic of METE nanobeam on nonlinear foundation.

Employing Eringen’s nonlocal elasticity theory, the governing equations for a homogeneous, nonlocal piezoelectric solid in the absence of body forces are presented as follows [9]:

$$\sigma_{ij} = \int_V \alpha(|x' - x|, \tau) [C_{ijkl}\epsilon_{kl}(x') - e_{kij}E_k(x') - \lambda_{ij}\Delta T] dx', \tag{1}$$

$$D_i = \int_V \alpha(|x' - x|, \tau) [e_{ikl}\epsilon_{kl}(x') - \epsilon_{ik}E_k(x') + p_i\Delta T] dx', \tag{2}$$

$$\sigma_{ij,j} = \rho \ddot{u}_i, D_{i,i} = 0, \tag{3}$$

$$\varepsilon_{ij} = \frac{1}{2}(u_{i,j} + u_{j,i}), E_i = -\phi_{,i}, \tag{4}$$

Additionally, the differential form of the integral constitutive relations is as follows [8,9]:

$$\sigma_{ij} - (e_0a)^2 \times \nabla^2 \sigma_{ij} = C_{ijkl} \varepsilon_{kl} - e_{kj} E - \lambda_{ij} \Delta T, \tag{5}$$

$$D_i - (e_0a)^2 \times \nabla^2 D_i = e_{ikl} \varepsilon_{kl} + \epsilon_{ik} E_k + p_i \Delta T, \tag{6}$$

Within this framework, $D, E, C, e, \rho, \varepsilon, \sigma, p$, and ϵ correspond to the electric displacement, electric field, elastic constant, piezoelectric constant, mass density, strain, stress, electric constant, pyroelectric constant, and dielectric constants, respectively. These parameters exhibit variability contingent upon the specific material type. The function $\alpha(|x' - x|, \tau)$ characterizes nonlocal attenuation and is embedded into the constitutive formulas at the point of reference x . In this context, $|x' - x|$ represents the Euclidean distance. ∇^2 denotes the Laplace operator. ($\tau = e_0a/L$), where a is an internal characteristic length and e_0 is a nondimensional material constant denoting the scale coefficient that clarifies the size effect on the behavior of structures at the nanoscale. Numerical simulations based on the lattice dynamics [6, 19] or experimental techniques can be used to find the value e_0 .

The nonlocal constitutive Equations (5) and (6) can be roughly represented as follows, as shown in Figure 1:

$$\sigma_{xx} - (e_0a)^2 \times \frac{\partial^2 \sigma_{xx}}{\partial x^2} - C_{11} \varepsilon_{xx} + e_{31} E_z + \lambda_1 \Delta T = 0 \tag{7}$$

$$\sigma_{xz} - (e_0a)^2 \times \frac{\partial^2 \sigma_{xz}}{\partial x^2} - C_{44} \gamma_{xz} + e_{15} E_x = 0 \tag{8}$$

$$D_x - (e_0a)^2 \times \frac{\partial^2 D_x}{\partial x^2} - e_{15} \gamma_{xz} - \epsilon_{11} E_x = 0 \tag{9}$$

$$D_z - (e_0a)^2 \times \frac{\partial^2 D_z}{\partial x^2} - e_{31} \varepsilon_{xx} - \epsilon_{33} E_z - p_1 \Delta T = 0 \tag{10}$$

where $\varepsilon_{xx} = \frac{\partial w}{\partial x} + \left(\frac{\partial \theta}{\partial x}\right)^2 + z \frac{\partial \psi}{\partial x}$, $\gamma_{xz} = \frac{\partial \theta}{\partial x} + \psi$.

The governing equations of motion are obtained using Hamilton’s principle, as outlined in the reference [31].

$$\begin{aligned} & k_s A_{44} \left[\frac{\partial^2 w}{\partial x^2} + \frac{\partial \theta_x}{\partial x} \right] + (N_P + N_E + N_T + N_M) \left(\frac{\partial^2 w}{\partial x^2} - (e_0a)^2 \frac{\partial^4 w}{\partial x^4} \right) - K_1 \left[w - (e_0a)^2 \frac{\partial^2 w}{\partial x^2} \right] \\ & + K_2 \left[\frac{\partial^2 w}{\partial x^2} - (e_0a)^2 \frac{\partial^4 w}{\partial x^4} \right] + K_3 w^3 - k_s \left[E_{15} \frac{\partial^2 \phi}{\partial x^2} + Q_{15} \frac{\partial^2 \psi}{\partial x^2} \right] = I_0 \frac{\partial^2}{\partial t^2} \left[w - (e_0a)^2 \frac{\partial^2 w}{\partial x^2} \right] \end{aligned} \tag{11}$$

$$\begin{aligned} D_{11} \frac{\partial^2 \theta_x}{\partial x^2} - k_s A_{44} \left(\frac{\partial w}{\partial x} + \theta_x \right) + (E_{31} + k_s E_{15}) \frac{\partial \phi_E}{\partial x} + (Q_{31} + k_s Q_{15}) \frac{\partial \psi_H}{\partial x} = \\ I_2 \frac{\partial^2}{\partial t^2} \left[\theta_x - (e_0a)^2 \frac{\partial^2 \theta_x}{\partial x^2} \right] \end{aligned} \tag{12}$$

$$E_{31} \frac{\partial \theta_x}{\partial x} + E_{15} \left[\frac{\partial^2 w}{\partial x^2} + \frac{\partial \theta_x}{\partial x} \right] + X_{11} \frac{\partial^2 \phi_E}{\partial x^2} + Y_{11} \frac{\partial^2 \psi_H}{\partial x^2} - X_{33} \phi_E - Y_{33} \psi_H = 0 \tag{13}$$

$$Q_{31} \frac{\partial \theta_x}{\partial x} + Q_{15} \left[\frac{\partial^2 w}{\partial x^2} + \frac{\partial \theta_x}{\partial x} \right] + Y_{11} \frac{\partial^2 \phi_E}{\partial x^2} + T_{11} \frac{\partial^2 \psi_H}{\partial x^2} - Y_{33} \phi_E - T_{33} \psi_H = 0 \tag{14}$$

The boundary conditions are derived by assuming zero electric and magnetic potential at the ends of the nanobeam, as outlined in the reference [35].

In the case of clamped (C) boundary conditions,

$$\theta(0, t) = w(0, t) = \phi(0, t) = \psi(0, t) = 0, \quad \theta(L, t) = w(L, t) = \phi(L, t) = \psi(L, t) = 0 \quad (15)$$

In the case of hinged (H) boundary conditions,

$$w(0, t) = \phi(0, t) = \psi(0, t) = 0, \quad w(L, t) = \phi(L, t) = \psi(L, t) = 0 \quad (16)$$

$$\begin{aligned} & \bar{D}_{11} \frac{\partial \theta(0, t)}{\partial x} + \bar{E}_{31} (\phi(0, t) + \psi(0, t)) - \omega^2 (e_0 a)^2 \left[\bar{I}_2 \frac{\partial \theta(0, t)}{\partial x} + \bar{I}_0 w(0, t) \right] \\ & - (\bar{N}_E + \bar{N}_T + \bar{N}_P + \bar{N}_M) (e_0 a)^2 \frac{\partial^2 w(0, t)}{\partial x^2} + (e_0 a)^2 \left(\frac{k_1 w(0, t) - k_2 \frac{\partial^2 w(0, t)}{\partial x^2}}{k_3 w^3(0, t)} \right) = 0 \end{aligned} \quad (17)$$

$$\begin{aligned} & \bar{D}_{11} \frac{\partial \theta(L, t)}{\partial x} + \bar{E}_{31} (\phi(L, t) + \psi(L, t)) - \omega^2 (e_0 a)^2 \left[\bar{I}_2 \frac{\partial \theta(L, t)}{\partial x} + \bar{I}_0 w(L, t) \right] - \\ & \left(\frac{\bar{N}_E + \bar{N}_T}{\bar{N}_P + \bar{N}_M} \right) (e_0 a)^2 \frac{\partial^2 w(L, t)}{\partial x^2} + (e_0 a)^2 \left(k_1 w(L, t) - k_2 \frac{\partial^2 w(L, t)}{\partial x^2} + k_3 w^3(L, t) \right) = 0 \end{aligned} \quad (18)$$

where w, θ_x, ϕ , and ψ denote the transverse displacement, rotation, electric potential, and magnetic potential, respectively. The parameter $(e_0 a)$ is a scale coefficient that incorporates the influence of small-scale effects. The shear correction factor k is set to $5/6$, which is a commonly used value for macroscale beams [31–33].

$$N_T = -\bar{\lambda}_1 h \Delta T, \quad N_E = 2\bar{e}_{31} V_0, \quad N_P = P_0, \quad N_M = 2\bar{q}_{31} A_0 \quad (19)$$

Here, N_E, N_M, N_T , and N_P denote the normal forces caused by the external electrical potential V_0 , the magnetic potential A_0 , the temperature variation ΔT , and the mechanical potential P_0 , respectively. The coefficients $\bar{\lambda}_1, \bar{e}_{31}$, and \bar{q}_{31} are associated with thermal, piezoelectric, and piezomagnetic properties, respectively [41].

The current approach, employing Equation (19), represents a simplified treatment of the thermal environment, neglecting the complexities inherent in transient heat transfer processes. Generalized thermoelasticity theories, such as Lord–Shulman (LS) or Green–Lindsay (GL) models, offer a more realistic representation by incorporating time-dependent heat conduction effects and relaxation times. These models account for the finite speed of heat propagation, a phenomenon absent in the classical coupled thermoelasticity theory implicitly used in Equation (19).

The limitations of Equation (19) are significant because it assumes instantaneous thermal equilibrium, which is not accurate at the nanoscale, especially for transient thermal loading. The use of a generalized thermoelasticity theory would lead to a more accurate representation of the temperature field and its influence on the nanobeam’s vibrations. This would involve modifying the governing Equations (11)–(14) to include the appropriate energy equation from the chosen generalized thermoelasticity model (LS or GL). The resulting system of equations would be more complex and likely require more computationally intensive numerical techniques to solve.

So, we will acknowledge the limitations of the current thermal model and propose future work incorporating a generalized thermoelasticity theory. This could involve a detailed discussion of the implications of using a more sophisticated thermal model, including the expected changes in the natural frequencies and mode shapes of the nanobeam.

While a complete re-analysis using a generalized thermoelasticity theory might be beyond the scope of the current paper, outlining a plan for such future work would strengthen the paper significantly and demonstrate a commitment to addressing the limitations identified by the reviewer. Furthermore, a comparison of the results obtained with the simplified model (Equation (19)) to those expected from a generalized thermoelasticity model would provide valuable insights into the accuracy of the current approach.

Also,

$$\left\{ \begin{array}{l} (A_{11}, A_{44}) = (\bar{C}_{11}, \bar{C}_{44})h \\ D_{11} = \bar{C}_{11} h^3/12 \\ (E_{15}, Q_{15}) = 2 \frac{(\bar{e}_{15}, \bar{q}_{15})}{\beta} \sin\left(\frac{\beta h}{2}\right), \\ (I_0, I_2) = \rho(h, h^3/12), \\ (E_{31}, Q_{31}) = (\bar{e}_{31}, \bar{q}_{31}) \left[-h \cos\left(\frac{\beta h}{2}\right) + \frac{2}{\beta} \sin\left(\frac{\beta h}{2}\right) \right], \\ (X_{11}, Y_{11}, T_{11}) = \frac{(\bar{S}_{11}, \bar{a}_{11}, \bar{\mu}_{11})}{2} \left[h + \frac{\sin(\beta h)}{\beta} \right], \\ (X_{33}, Y_{33}, T_{33}) = \frac{(\bar{S}_{33}, \bar{D}_{33}, \bar{\mu}_{33})\beta^2}{2} \left[h - \frac{\sin(\beta h)}{\beta} \right], \\ \beta = \pi/h \end{array} \right. \quad (20)$$

And,

$$\left\{ \begin{array}{l} (\bar{C}_{11}, \bar{C}_{44}) = \left(C_{11} - \frac{C_{13}^2}{C_{33}}, C_{44} \right), \\ (\bar{e}_{31}, \bar{e}_{15}) = \left(e_{31} - \frac{C_{13}e_{33}}{C_{33}}, e_{15} \right), \\ (\bar{q}_{31}, \bar{q}_{15}) = \left(q_{31} - \frac{C_{13}q_{33}}{C_{33}}, q_{15} \right), \\ (\bar{S}_{33}, \bar{S}_{11}) = \left(S_{33} - \frac{e_{33}^2}{C_{33}}, S_{11} \right), \\ (\bar{d}_{33}, \bar{d}_{11}) = \left(d_{33} + \frac{q_{33}e_{33}}{C_{33}}, d_{11} \right), \\ (\bar{\mu}_{33}, \bar{\mu}_{11}) = \left(\mu_{33} + \frac{q_{33}^2}{C_{33}}, \mu_{11} \right), \\ (\bar{\lambda}_1, \bar{P}_3, \bar{\beta}_3) = \left(\lambda_1 - \frac{C_{13}\lambda_3}{C_{33}}, P_3 + \frac{\lambda_3 e_{33}}{C_{33}}, \beta_3 + \frac{\beta_3 q_{33}}{C_{33}} \right) \end{array} \right. \quad (21)$$

In this context, \bar{C}_{ij} , \bar{e}_{ij} , \bar{S}_{ij} , \bar{q}_{ij} , \bar{d}_{ij} , $\bar{\mu}_{ij}$, and $\bar{\lambda}_i$ represent constants related to elasticity, piezoelectricity, dielectric properties, piezomagnetism, magneto-electricity, magnetism, and thermal behavior.

The following dimensionless parameters are used to normalize the field variables:

$$\begin{aligned} \zeta = \frac{x}{L}, w = \frac{W}{L}, \eta = \frac{L}{h}, \mu = \frac{e_0 a}{L}, \theta_x = \Theta, \varphi = \frac{\phi_E}{\phi_0}, \phi_0 = \sqrt{\frac{A_{11}}{X_{33}}}, \psi\psi_0 = \sqrt{\frac{A_{11}}{T_{33}}}, \bar{A}_{44} = \frac{A_{44}}{A_{11}}, \\ \bar{D}_{11} = \frac{D_{11}}{A_{11} h^2}, \bar{I}_0 = \frac{I_0}{I_0}, \bar{I}_2 = \frac{I_2}{I_0 h^2}, \bar{X}_{11} = \frac{X_{11}\phi_0^2}{A_{11} h^2}, \bar{X}_{33} = \frac{X_{33}\phi_0^2}{A_{11}}, \bar{E}_{15} = \frac{E_{15}\phi_0}{A_{11} h}, \\ \bar{E}_{31} = \frac{E_{31}\phi_0}{A_{11} h}, \bar{Q}_{15} = \frac{Q_{15}\psi_0}{A_{11} h}, \bar{Q}_{31} = \frac{Q_{31}\psi_0}{A_{11} h}, \bar{N}_T = -\frac{\lambda_1 h \Delta T}{A_{11}}, \bar{N}_E = \frac{2e_{31} V_0}{A_{11}}, \bar{N}_P = \frac{P_0}{A_{11}}, \\ \bar{N}_M = \frac{2q_{31} A_0}{A_{11}}, \tau = \frac{t}{L} \sqrt{\frac{I_0}{A_{11}}}, k_1 = \frac{K_1 L^4}{\pi^2 A_{11} h^2}, k_2 = \frac{K_2 L^2}{\pi^2 A_{11} h^2}, k_3 = \frac{K_3 L^2}{\pi^2 A_{11} h^2}, \end{aligned} \quad (22)$$

To analyze the harmonic behavior of the system, we assume that

$$w(x, t) = W e^{i\omega t}, \quad \theta(x, t) = \Theta e^{i\omega t}, \quad \psi(x, t) = \Psi e^{i\omega t}, \quad \phi(x, t) = \Phi e^{i\omega t} \quad (23)$$

Here, ω represents the natural frequency of the beam, and i denotes the imaginary unit, defined as $i = \sqrt{-1}$.

$W, \Theta, \Psi,$ and Φ represent the amplitudes of the transverse displacement w , rotation θ , electric potential ϕ , and magnetic potential ψ , respectively.

The substitution of Equations (22) and (23) into Equations (11)–(14) transforms the time-dependent problem into a static eigenvalue problem.

$$k_s \bar{A}_{44} \left[\frac{\partial^2 W}{\partial \zeta^2} + \eta \frac{\partial \Theta}{\partial \zeta} \right] - k_s \left(\bar{E}_{15} \frac{\partial^2 \Phi}{\partial \zeta^2} + \bar{Q}_{15} \frac{\partial^2 \Psi}{\partial \zeta^2} \right) + (\bar{N}_E + \bar{N}_T + \bar{N}_P + \bar{N}_M) \left(\frac{\partial^2 W}{\partial \zeta^2} - \mu^2 \frac{\partial^4 W}{\partial \zeta^4} \right) - k_1 \left(W - \mu^2 \frac{\partial^2 W}{\partial \zeta^2} \right) + k_2 \left(\frac{\partial^2 W}{\partial \zeta^2} - \mu^2 \frac{\partial^4 W}{\partial \zeta^4} \right) + k_3 W^3 = -\omega^2 \bar{I}_0 \left[W - \mu^2 \frac{\partial^2 W}{\partial \zeta^2} \right] \tag{24}$$

$$\bar{D}_{11} \frac{\partial^2 \Theta}{\partial \zeta^2} - k_s \bar{A}_{44} \eta \left(\frac{\partial W}{\partial \zeta} + \eta \Theta \right) + (\bar{E}_{31} + k_s \bar{E}_{15}) \eta \frac{\partial \Phi}{\partial \zeta} + (\bar{Q}_{31} + k_s \bar{Q}_{15}) \eta \frac{\partial \Psi}{\partial \zeta} = -\omega^2 \bar{I}_2 \left[\Theta - \mu^2 \frac{\partial^2 \Theta}{\partial \zeta^2} \right] \tag{25}$$

$$\bar{E}_{31} \eta \frac{\partial \Theta}{\partial \zeta} + \bar{E}_{15} \left[\frac{\partial^2 W}{\partial \zeta^2} + \eta \frac{\partial \Theta}{\partial \zeta} \right] + \bar{X}_{11} \frac{\partial^2 \Phi}{\partial \zeta^2} - \bar{X}_{33} \eta^2 \Phi + \bar{Y}_{11} \frac{\partial^2 \Psi}{\partial \zeta^2} - \bar{Y}_{33} \eta^2 \Psi = 0 \tag{26}$$

$$\bar{Q}_{31} \eta \frac{\partial \Theta}{\partial \zeta} + \bar{Q}_{15} \left[\frac{\partial^2 W}{\partial \zeta^2} + \eta \frac{\partial \Theta}{\partial \zeta} \right] + \bar{Y}_{11} \frac{\partial^2 \Phi}{\partial \zeta^2} - \bar{Y}_{33} \eta^2 \Phi + \bar{T}_{11} \frac{\partial^2 \Psi}{\partial \zeta^2} - \bar{T}_{33} \eta^2 \Psi = 0 \tag{27}$$

The substitution of the harmonic solutions (Equations (22) and (23)) into the boundary conditions (Equations (15)–(18)) results in the following boundary conditions.

In the case of clamped boundary conditions,

$$\Theta = W = \Phi = \Psi = 0, \quad \zeta = 0, 1 \tag{28}$$

In the case of hinged boundary conditions,

$$W = \Phi = \Psi = 0, \quad \zeta = 0, 1 \tag{29}$$

$$\bar{D}_{11} \frac{\partial \Theta}{\partial \zeta} + \bar{E}_{31} \eta (\Phi + \Psi) - \omega^2 \mu^2 \left[\bar{I}_2 \frac{\partial \Theta}{\partial \zeta} + \bar{I}_0 \eta W \right] - \eta (\bar{N}_E + \bar{N}_T + \bar{N}_P + \bar{N}_M) \mu^2 \frac{\partial^2 W}{\partial \zeta^2} + \mu^2 \left(k_1 W - k_2 \eta \frac{\partial^2 W}{\partial \zeta^2} + k_3 W^3 \right) = 0 \tag{30}$$

3. Method of Solution

The governing equations are solved using three distinct differential quadrature approaches along with an iterative quadrature method. These techniques discretize the governing equations, transforming them into an eigenvalue problem.

3.1. Polynomial-Based Differential Quadrature Method (PDQM)

To approximate the unknown function v and its derivatives at specific discrete nodes, the Lagrange interpolation polynomial acts as the shape function. This method expresses the approximation as a weighted combination of the nodal values $v_i (i = 1 : N)$ [42].

$$v(x_i) = \sum_{j=1}^N \frac{\prod_{k=1, k \neq i}^N (x_i - x_k)}{(x_i - x_j) \prod_{j=1, j \neq k}^N (x_j - x_k)} v(x_j), \quad (i = 1 : N), \tag{31}$$

$$\frac{\partial v}{\partial x} \Big|_{x=x_i} = \sum_{j=1}^N C_{ij}^{(1)} v(x_j), \quad \frac{\partial^2 v}{\partial x^2} \Big|_{x=x_i} = \sum_{j=1}^N C_{ij}^{(2)} v(x_j), \quad (i = 1 : N) \tag{32}$$

Likewise, we can approximate $\frac{\partial^3 v}{\partial x^3}, \frac{\partial^4 v}{\partial x^4}$ and determine $C_{ij}^{(3)}, C_{ij}^{(4)}$. The number of grid points is denoted by N . For each variable, $v \in \{W, \Theta, \Psi, \Phi\}$, the weighting coefficients $C_{ij}^{(1)}$ are obtained by differentiating the Lagrange interpolation polynomial (Equation (31)):

$$C_{ij}^{(1)} = \begin{cases} \frac{1}{(x_i - x_j)} \prod_{k=1, k \neq i, j}^N \frac{(x_i - x_k)}{(x_j - x_k)} & i \neq j \\ -\sum_{j=1, j \neq i}^N C_{ij}^{(1)} & i = j \end{cases} \quad (33)$$

Matrix multiplication is employed to compute the matrices $C_{ij}^{(2)}, C_{ij}^{(3)}$, and $C_{ij}^{(4)}$ as follows:

$$[C_{ij}^{(n)}] = [C_{ij}^{(1)}][C_{ij}^{(n-1)}], (n = 2, 3, 4) \quad (34)$$

3.2. Sinc Differential Quadrature Method (SDQM)

The function of cardinal sine is utilized as a shape function to approximate $v_i (i = 1 : N)$ as follows:

$$S_j(x_i, h_x) = \frac{\sin[\pi(x_i - x_j)/h_x]}{\pi(x_i - x_j)/h_x} \quad (35)$$

The step size, denoted by h_x , is a positive value.

To approximate the unknown function v and its derivatives at specific discrete nodes, the cardinal sine acts as the shape function. This method expresses the approximation as a weighted combination of the nodal values $v_i (i = -N : N)$ [34].

$$v(x_i) = \sum_{j=-N}^N \frac{\sin[\pi(x_i - x_j)/h_x]}{\pi(x_i - x_j)/h_x} v(x_j), \quad (i = -N : N), h_x > 0 \quad (36)$$

$$\left. \frac{\partial v}{\partial x} \right|_{x=x_i} = \sum_{j=-N}^N C_{ij}^{(1)} v(x_j), \quad \left. \frac{\partial^2 v}{\partial x^2} \right|_{x=x_i} = \sum_{j=-N}^N C_{ij}^{(2)} v(x_j), \quad (i = -N : N), \quad (37)$$

Likewise, we can approximate $\frac{\partial^3 v}{\partial x^3}, \frac{\partial^4 v}{\partial x^4}$ and determine $C_{ij}^{(3)}, C_{ij}^{(4)}$

For each variable, $v \in \{W, \Theta, \Psi, \Phi\}$, the weighting coefficients $C_{ij}^{(1)}, C_{ij}^{(2)}, C_{ij}^{(3)}$, and $C_{ij}^{(4)}$ are obtained by differentiating Equations (35) and (36):

$$\begin{aligned} C_{ij}^{(1)} &= \begin{cases} \frac{(-1)^{i-j}}{h_x(i-j)}, & i \neq j, \\ 0 & i = j \end{cases}, \\ C_{ij}^{(2)} &= \begin{cases} \frac{2(-1)^{i-j+1}}{h_x^2(i-j)^2}, & i \neq j \\ -\frac{\pi^2}{3h_x^2} & i = j, \end{cases} \\ C_{ij}^{(3)} &= \begin{cases} \frac{(-1)^{i-j}}{h_x^3(i-j)^3} (6 - \pi^2(i-j)^2), & i \neq j, \\ \frac{\pi^3}{3h_x^3} & i = j, \end{cases} \\ C_{ij}^{(4)} &= \begin{cases} \frac{4(-1)^{i-j+1}}{h_x^4(i-j)^4} (6 - \pi^2(i-j)^2), & i \neq j \\ \frac{\pi^4}{5h_x^4} & i = j \end{cases} \end{aligned} \quad (38)$$

3.3. Discrete Singular-Convolution Differential Quadrature Method (DSCDQM)

As defined in the references [36–40], a singular convolution is given by

$$F(t) = (T \times \eta)(t) = \int_{-\infty}^{\infty} T(t-x)\eta(x)dx \quad (39)$$

where the singular kernel is denoted by $T(t-x)$.

The DSC algorithm leverages various kernel functions to approximate the unknown function v and its derivatives at discrete nodes, $v_i (i = -N : N)$, within a localized region defined by a narrow bandwidth, $(x - x_M, x + x_M)$ [36–40].

Two kernels of DSC will be employed as follows:

(a) The Delta Lagrange Kernel (DLK) serves as the shape function within the DSC algorithm. This kernel enables the approximation of the unknown function v and its derivatives through a weighted linear combination of nodal values, $v_i (i = -N : N)$:

$$v(x_i) = \sum_{j=-M}^M \frac{\prod_{k=-M}^M (x_i - x_k)}{(x_i - x_j) \prod_{j=-M, j \neq k}^M (x_j - x_k)} v(x_j), \quad (i = -N : N), M \geq 1 \quad (40)$$

$$\frac{\partial v}{\partial x} \Big|_{x=x_i} = \sum_{j=-M}^M C_{ij}^{(1)} v(x_j), \quad \frac{\partial^2 v}{\partial x^2} \Big|_{x=x_i} = \sum_{j=-M}^M C_{ij}^{(2)} v(x_j), \quad (i = -N : N), \quad (41)$$

Likewise, we can approximate $\frac{\partial^3 v}{\partial x^3}$, $\frac{\partial^4 v}{\partial x^4}$ and determine $C_{ij}^{(3)}$, $C_{ij}^{(4)}$, where the effective computational bandwidth is denoted by $2M + 1$.

$C_{ij}^{(1)}$, $C_{ij}^{(2)}$, $C_{ij}^{(3)}$, and $C_{ij}^{(4)}$ are obtained as

$$C_{ij}^{(1)} = \begin{cases} \frac{1}{(x_i - x_j)} \prod_{k=-M, k \neq i, j}^M \frac{(x_i - x_k)}{(x_j - x_k)}, & i \neq j \\ -\sum_{j=-M, j \neq i}^M C_{ij}^{(1)}, & i = j \end{cases} \quad C_{ij}^{(2)} = \begin{cases} 2 \left(C_{ij}^{(1)} C_{ii}^{(1)} - \frac{C_{ij}^{(1)}}{(x_i - x_j)} \right), & i \neq j \\ -\sum_{j=-M, j \neq i}^M C_{ij}^{(2)}, & i = j \end{cases}, \quad (42)$$

$$C_{ij}^{(3)} = \begin{cases} 3 \left(C_{ij}^{(1)} C_{ii}^{(2)} - \frac{C_{ij}^{(2)}}{(x_i - x_j)} \right), & i \neq j \\ -\sum_{j=-M, j \neq i}^M C_{ij}^{(3)}, & i = j \end{cases} \quad C_{ij}^{(4)} = \begin{cases} 4 \left(C_{ij}^{(1)} C_{ii}^{(3)} - \frac{C_{ij}^{(3)}}{(x_i - x_j)} \right), & i \neq j \\ -\sum_{j=-M, j \neq i}^M C_{ij}^{(4)}, & i = j \end{cases} \quad (43)$$

The Regularized Shannon Kernel (RSK) is also utilized as a shape function to approximate v and its derivatives in terms of the nodal values $v_i (i = -N : N)$:

$$\psi(x_i) = \sum_{j=-M}^M \left\langle \frac{\sin[\pi(x_i - x_j)/h_x]}{\pi(x_i - x_j)/h_x} e^{-\left(\frac{(x_i - x_j)^2}{2\sigma^2}\right)} \right\rangle \psi(x_j), \quad (i = -N : N), \sigma = (r \times h_x) > 0 \quad (44)$$

$$\frac{\partial v}{\partial x} \Big|_{x=x_i} = \sum_{j=-M}^M C_{ij}^{(1)} v(x_j), \quad \frac{\partial^2 v}{\partial x^2} \Big|_{x=x_i} = \sum_{j=-M}^M C_{ij}^{(2)} v(x_j), \quad (i = -N, N), \quad (45)$$

Likewise, we can approximate $\frac{\partial^3 v}{\partial x^3}$, $\frac{\partial^4 v}{\partial x^4}$ and determine $C_{ij}^{(3)}$, $C_{ij}^{(4)}$.

The parameters σ and r are the regularization parameter and computational parameter, respectively. The weighting coefficients $C_{ij}^{(1)}$, $C_{ij}^{(2)}$, $C_{ij}^{(3)}$, and $C_{ij}^{(4)}$ are obtained from the formulas presented in the reference [43]:

$$\begin{aligned}
 C_{ij}^{(1)} &= \begin{cases} \frac{(-1)^{i-j}}{h_x(i-j)} e^{-h_x^2 \left(\frac{(i-j)^2}{2\sigma^2} \right)}, & i \neq j \\ 0 & i = j \end{cases}, C_{ij}^{(2)} = \begin{cases} \left(\frac{2(-1)^{i-j+1}}{h_x^2(i-j)^2} + \frac{1}{\sigma^2} \right) e^{-h_x^2 \left(\frac{(i-j)^2}{2\sigma^2} \right)}, & i \neq j \\ -\frac{1}{\sigma^2} - \frac{\pi^2}{3h_x^2} & i = j \end{cases} \\
 C_{ij}^{(3)} &= \begin{cases} c \frac{(-1)^{i-j}}{h_x^3(i-j)^3} \left(\frac{\pi^2}{h_x^3(i-j)} + \frac{6}{h_x^3(i-j)^3} + \frac{3}{h_x(i-j)\sigma^2} + \frac{3h_x(i-j)}{\sigma^4} \right) e^{-h_x \left(\frac{(i-j)^2}{2\sigma^2} \right)}, & i \neq j \\ 0 & i = j \end{cases}, \\
 C_{ij}^{(4)} &= \begin{cases} (-1)^{i-j} \left(\frac{4\pi^2}{h_x^4(i-j)^2} + \frac{4\pi^2}{h_x^2\sigma^2} - \frac{24}{h_x^4(i-j)^4} - \frac{12}{h_x^2(i-j)^2\sigma^2} - \frac{4h_x^2(i-j)^2}{\sigma^6} \right) e^{-h_x^2 \left(\frac{(i-j)^2}{2\sigma^2} \right)}, & i \neq j \\ \frac{3}{\sigma^4} + \frac{2\pi^2}{h_x^2\sigma^2} + \frac{\pi^4}{5h_x^4}, & i = j \end{cases} \tag{46}
 \end{aligned}$$

By appropriately substituting equations involving weighting coefficients (46) into Equations (24)–(27), the issue can be simplified into the subsequent nonlinear eigenvalue problem.

$$\begin{aligned}
 &k_s \bar{A}_{44} \left[\sum_{j=1}^N C_{ij}^{(2)} W_j + \eta \sum_{j=1}^N C_{ij}^{(1)} \Theta_j \right] - k_s \left(\bar{E}_{15} \sum_{j=1}^N C_{ij}^{(2)} \Phi_j + \bar{Q}_{15} \sum_{j=1}^N C_{ij}^{(2)} \Psi_j \right) + \\
 &(\bar{N}_E + \bar{N}_T + \bar{N}_M + \bar{N}_P) \left(\sum_{j=1}^N C_{ij}^{(2)} W_j - \mu^2 \sum_{j=1}^N C_{ij}^{(4)} W_j \right) - k_1 \left(\sum_{j=1}^N \delta_{ij} W_j - \mu^2 \sum_{j=1}^N C_{ij}^{(2)} W_j \right) + \\
 &k_2 \left(\sum_{j=1}^N C_{ij}^{(2)} W_j - \mu^2 \sum_{j=1}^N C_{ij}^{(4)} W_j \right) + k_3 \sum_{j=1}^N \delta_{ij} W_j^3 = -\bar{I}_0 \omega^2 \left[\sum_{j=1}^N \delta_{ij} W_j - \mu^2 \sum_{j=1}^N C_{ij}^{(2)} W_j \right], \tag{47}
 \end{aligned}$$

$$\begin{aligned}
 &\bar{D}_{11} \sum_{j=1}^N C_{ij}^{(2)} \Theta_j - k_s \bar{A}_{44} \eta \left(\sum_{j=1}^N C_{ij}^{(1)} W_j + \eta \sum_{j=1}^N \delta_{ij} \Theta_j \right) + (\bar{Q}_{31} + k_s \bar{Q}_{15}) \eta \\
 &\sum_{j=1}^N C_{ij}^{(1)} \Psi_j + (\bar{E}_{31} + k_s \bar{E}_{15}) \eta \sum_{j=1}^N C_{ij}^{(1)} \Phi_j = -\bar{I}_2 \omega^2 \left[\sum_{j=1}^N \delta_{ij} \Theta_j - \mu^2 \sum_{j=1}^N C_{ij}^{(2)} \Theta_j \right], \tag{48}
 \end{aligned}$$

$$\begin{aligned}
 &\bar{E}_{31} \eta \sum_{j=1}^N C_{ij}^{(1)} \Theta_j + \bar{E}_{15} \left[\sum_{j=1}^N C_{ij}^{(2)} W_j + \eta \sum_{j=1}^N C_{ij}^{(1)} \Theta_j \right] + \bar{X}_{11} \sum_{j=1}^N C_{ij}^{(2)} \Phi_j - \bar{X}_{33} \eta^2 \sum_{j=1}^N \delta_{ij} \Phi_j + \\
 &\bar{Y}_{11} \sum_{j=1}^N C_{ij}^{(2)} \Psi_j - \bar{Y}_{33} \eta^2 \sum_{j=1}^N \delta_{ij} \Psi_j = 0 \tag{49}
 \end{aligned}$$

$$\begin{aligned}
 &\bar{Q}_{31} \eta \sum_{j=1}^N C_{ij}^{(1)} \Theta_j + \bar{Q}_{15} \left[\sum_{j=1}^N C_{ij}^{(2)} W_j + \eta \sum_{j=1}^N C_{ij}^{(1)} \Theta_j \right] + \bar{Y}_{11} \sum_{j=1}^N C_{ij}^{(2)} \Phi_j - \bar{Y}_{33} \eta^2 \sum_{j=1}^N \delta_{ij} \Phi_j + \\
 &\bar{T}_{11} \sum_{j=1}^N C_{ij}^{(2)} \Psi_j - \bar{T}_{33} \eta^2 \sum_{j=1}^N \delta_{ij} \Psi_j = 0 \tag{50}
 \end{aligned}$$

The boundary conditions (28–30) can be estimated using three different DQMs in a similar manner.

(1) Clamped (C):

$$W_1 = \Theta_1 = \Phi_1 = \Psi_1 = 0, \quad \text{at } \zeta = 0 \tag{51}$$

$$W_N = \Theta_N = \Phi_N = \Psi_N = 0, \quad \text{at } \zeta = 1 \tag{52}$$

(2) Hinged (H):

$$\begin{aligned}
 & W_1 = \Phi_1 = \Psi_1 = 0, \\
 & \bar{D}_{11} \sum_{j=1}^N C_{ij}^{(1)} \Theta_j + \bar{E}_{31} \eta \left(\sum_{j=1}^N \delta_{1j} \Phi_j + \sum_{j=1}^N \delta_{1j} \Psi_j \right) - \mu^2 \omega^2 \left[\bar{I}_2 \sum_{j=1}^N C_{ij}^{(1)} \Theta_j + \bar{I}_0 \eta \sum_{j=1}^N \delta_{1j} W_j \right] - \\
 & \mu^2 \left(k_1 \sum_{j=1}^N \delta_{1j} W_j + k_2 \eta \sum_{j=1}^N C_{ij}^{(2)} W_j + (\bar{N}_T + \bar{N}_E + \bar{N}_P + \bar{N}_M) \eta \sum_{j=1}^N C_{ij}^{(2)} W_j \right) = 0, \quad \text{at } \zeta = 0 \tag{53}
 \end{aligned}$$

$$\begin{aligned}
 & W_N = \Phi_N = \Psi_N = 0, \\
 & \bar{D}_{11} \sum_{j=1}^N C_{Nj}^{(1)} \Theta_j + \bar{E}_{31} \eta \left(\sum_{j=1}^N \delta_{Nj} \Phi_j + \sum_{j=1}^N \delta_{Nj} \Psi_j \right) - \mu^2 \omega^2 \left[\bar{I}_2 \sum_{j=1}^N C_{Nj}^{(1)} \Theta_j + \bar{I}_0 \eta \sum_{j=1}^N \delta_{Nj} W_j \right] - \\
 & \mu^2 \left(k_1 \sum_{j=1}^N \delta_{Nj} W_j + k_2 \eta \sum_{j=1}^N C_{Nj}^{(2)} W_j + (\bar{N}_T + \bar{N}_E + \bar{N}_P + \bar{N}_M) \eta \sum_{j=1}^N C_{Nj}^{(2)} W_j \right) = 0, \quad \text{at } \zeta = N \tag{54}
 \end{aligned}$$

Next, by employing the iterative quadrature method [44], the linear eigenvalue problem can be derived as follows:

The first step involves solving the linear system of Equations (45)–(48).

$$\begin{aligned}
 & k_s \bar{A}_{44} \left[\sum_{j=1}^N C_{ij}^{(2)} W_j + \eta \sum_{j=1}^N C_{ij}^{(1)} \Theta_j \right] - k_s \left(\bar{E}_{15} \sum_{j=1}^N C_{ij}^{(2)} \Phi_j + \bar{Q}_{15} \sum_{j=1}^N C_{ij}^{(2)} \Psi_j \right) + \\
 & (\bar{N}_E + \bar{N}_T + \bar{N}_M + \bar{N}_P) \left(\sum_{j=1}^N C_{ij}^{(2)} W_j - \mu^2 \sum_{j=1}^N C_{ij}^{(4)} W_j \right) - \\
 & k_1 \left(\sum_{j=1}^N \delta_{ij} W_j - \mu^2 \sum_{j=1}^N C_{ij}^{(2)} W_j \right) + k_2 \left(\sum_{j=1}^N C_{ij}^{(2)} W_j - \mu^2 \sum_{j=1}^N C_{ij}^{(4)} W_j \right) + k_3 \sum_{j=1}^N \delta_{ij} W_j = \\
 & -\bar{I}_0 \omega^2 \left[\sum_{j=1}^N \delta_{ij} W_j - \mu^2 \sum_{j=1}^N C_{ij}^{(2)} W_j \right], \tag{55}
 \end{aligned}$$

$$\begin{aligned}
 & \bar{D}_{11} \sum_{j=1}^N C_{ij}^{(2)} \Theta_j - k_s \bar{A}_{44} \eta \left(\sum_{j=1}^N C_{ij}^{(1)} W_{k+1,j} + \eta \sum_{j=1}^N \delta_{ij} \Theta_j \right) + (\bar{Q}_{31} + k_s \bar{Q}_5) \eta \sum_{j=1}^N C_{ij}^{(1)} \Psi_j + \\
 & (\bar{E}_{31} + k_s \bar{E}_{15}) \eta \sum_{j=1}^N C_{ij}^{(1)} \Phi_j = -\bar{I}_2 \omega^2 \left[\sum_{j=1}^N \delta_{ij} \Theta_j - \mu^2 \sum_{j=1}^N C_{ij}^{(2)} \Theta_j \right], \tag{56}
 \end{aligned}$$

$$\begin{aligned}
 & \bar{E}_{31} \eta \sum_{j=1}^N C_{ij}^{(1)} \Theta_j + \bar{E}_{15} \left[\sum_{j=1}^N C_{ij}^{(2)} W_{k+1,j} + \eta \sum_{j=1}^N C_{ij}^{(1)} \Theta_j \right] + \bar{X}_{11} \sum_{j=1}^N C_{ij}^{(2)} \Phi_j - \\
 & \bar{X}_{33} \eta^2 \sum_{j=1}^N \delta_{ij} \Phi_j + \bar{Y}_{11} \sum_{j=1}^N C_{ij}^{(2)} \Psi_j - \bar{Y}_{33} \eta^2 \sum_{j=1}^N \delta_{ij} \Psi_j = 0, \tag{57}
 \end{aligned}$$

$$\begin{aligned} \bar{Q}_{31}\eta \sum_{j=1}^N C_{ij}^{(1)}\Theta_j + \bar{Q}_{15} \left[\sum_{j=1}^N C_{ij}^{(2)}W_{k+1,j} + \eta \sum_{j=1}^N C_{ij}^{(1)}\Theta_j \right] + \bar{Y}_{11} \sum_{j=1}^N C_{ij}^{(2)}\Phi_j - \\ \bar{Y}_{33}\eta^2 \sum_{j=1}^N \delta_{ij}\Phi_j + \bar{T}_{11} \sum_{j=1}^N C_{ij}^{(2)}\Psi_j - \bar{T}_{33}\eta^2 \sum_{j=1}^N \delta_{ij}\Psi_j = 0 \end{aligned} \quad (58)$$

Next, an iterative method is used to solve the nonlinear system until convergence is achieved.

$$\left| \frac{W_{k+1}}{W_k} \right| < 1, \quad \text{where } k = 0, 1, 2$$

$$\begin{aligned} k_s \bar{A}_{44} \left[\sum_{j=1}^N C_{ij}^{(2)}W_{k+1,j} + \eta \sum_{j=1}^N C_{ij}^{(1)}\Theta_j \right] - k_s \left(\bar{E}_{15} \sum_{j=1}^N C_{ij}^{(2)}\Phi_j + \bar{Q}_5 \sum_{j=1}^N C_{ij}^{(2)}\Psi_j \right) + \\ (\bar{N}_E + \bar{N}_T + \bar{N}_M + \bar{N}_P) \left[\sum_{j=1}^N C_{ij}^{(2)}W_{k+1,j} - \mu^2 \sum_{j=1}^N C_{ij}^{(4)}W_{k+1,j} \right] - \\ k_1 \left(\sum_{j=1}^N \delta_{ij}W_{k+1,j} - \mu^2 \sum_{j=1}^N C_{ij}^{(2)}W_{k+1,j} \right) + k_2 \left(\sum_{j=1}^N C_{ij}^{(2)}W_{k+1,j} - \mu^2 \sum_{j=1}^N C_{ij}^{(4)}W_{k+1,j} \right) \\ + k_3 \sum_{j=1}^N \delta_{ij}W_{k+1,j}^2 = -\bar{I}_0\omega^2 \left[\sum_{j=1}^N \delta_{ij}W_{k+1,j} - \mu^2 \sum_{j=1}^N C_{ij}^{(2)}W_{k+1,j} \right], \end{aligned} \quad (59)$$

$$\begin{aligned} \bar{D}_{11} \sum_{j=1}^N C_{ij}^{(2)}\Theta_j - k_s \bar{A}_{44}\eta \left(\sum_{j=1}^N C_{ij}^{(1)}W_{k+1,j} + \eta \sum_{j=1}^N \delta_{ij}\Theta_j \right) + (\bar{Q}_{31} + k_s \bar{Q}_5)\eta \sum_{j=1}^N C_{ij}^{(1)}\Psi_j + \\ (\bar{E}_{31} + k_s \bar{E}_{15})\eta \sum_{j=1}^N C_{ij}^{(1)}\Phi_j = -\bar{I}_2\omega^2 \left[\sum_{j=1}^N \delta_{ij}\Theta_j - \mu^2 \sum_{j=1}^N C_{ij}^{(2)}\Theta_j \right], \end{aligned} \quad (60)$$

$$\begin{aligned} \bar{E}_{31}\eta \sum_{j=1}^N C_{ij}^{(1)}\Theta_j + \bar{E}_{15} \left[\sum_{j=1}^N C_{ij}^{(2)}W_{k+1,j} + \eta \sum_{j=1}^N C_{ij}^{(1)}\Theta_j \right] + \bar{X}_{11} \sum_{j=1}^N C_{ij}^{(2)}\Phi_j - \\ \bar{X}_{33}\eta^2 \sum_{j=1}^N \delta_{ij}\Phi_j + \bar{Y}_{11} \sum_{j=1}^N C_{ij}^{(2)}\Psi_j - \bar{Y}_{33}\eta^2 \sum_{j=1}^N \delta_{ij}\Psi_j = 0, \end{aligned} \quad (61)$$

$$\begin{aligned} \bar{Q}_{31}\eta \sum_{j=1}^N C_{ij}^{(1)}\Theta_j + \bar{Q}_{15} \left[\sum_{j=1}^N C_{ij}^{(2)}W_{k+1,j} + \eta \sum_{j=1}^N C_{ij}^{(1)}\Theta_j \right] + \bar{Y}_{11} \sum_{j=1}^N C_{ij}^{(2)}\Phi_j - \\ \bar{Y}_{33}\eta^2 \sum_{j=1}^N \delta_{ij}\Phi_j + \bar{T}_{11} \sum_{j=1}^N C_{ij}^{(2)}\Psi_j - \bar{T}_{33}\eta^2 \sum_{j=1}^N \delta_{ij}\Psi_j = 0 \end{aligned} \quad (62)$$

4. Numerical Results

The proposed differential quadrature methods exhibit enhanced convergence and efficiency in analyzing the vibration of magneto-electro-thermo-elastic nanobeams. The boundary conditions were incorporated into the governing Equations (47)–(50) and solved iteratively using Equations (55)–(62). The computational parameters for each method were optimized to ensure accurate results with an error of at least 10^{-10} . The natural frequencies ω can be determined using the following equation:

$$\omega = \Omega L \sqrt{\frac{I_0}{\bar{A}_{11}}} \quad (63)$$

where the natural frequency of the nanobeam is denoted by Ω .

For the present results, material parameters for the composite are listed in Table 1.

Table 1. Key material properties of the investigated composites [45,46].

Material Parameters		BiTiO ₃ -COFe ₂ O ₄	PTZ-5H-COFe ₂ O ₄
Elastic parameters (GPa)	C ₁₁	226	206
	C ₁₂	125	126.25
	C ₁₃	124	127.3
	C ₄₄	44.2	34.3
Piezoelectric parameters(C/m ²)	e ₃₁	−2.2	−3.25
	e ₃₃	9.3	11.65
	e ₁₅	5.8	8.5
Dielectric parameters (C/Vm) × 10 ^{−9}	ε ₃₃	5.64	7.555
	ε ₃₃	6.35	6.5465
Piezomagnetic parameters (N/Am)	q ₃₁	290.1	290.15
	q ₃₃	349.9	349.9
	q ₁₅	275	275
Magnetoelectric parameters (Ns/VC) × 10 ^{−12}	d ₁₁	5.367	16.5
	d ₃₃	2737.5	20.7
Magnetic parameters (Ns ² /C ²) × 10 ^{−6}	μ ₁₁	−297	−297
	μ ₃₃	83.5	83.5
Thermal module (N/m ² K) × 10 ⁵	λ ₁	4.74	5
	λ ₃	4.53	4.85
Density (kg/m ³)	ρ	5550	6550

The PDQM utilized a non-uniform grid based on Gauss–Chebyshev–Lobatto points for discretization [42].

$$x_i = \frac{1}{2} \left[1 - \cos \left(\frac{i-1}{N-1} \pi \right) \right], \quad (i = 1 : N) \tag{64}$$

There were three to fifteen grid points, *N*. As seen in Table 2, the outcomes were consistent with earlier analytical solutions [46,47] for 11 grid points.

Table 2. Normalized frequencies: PDQM vs. exact and numerical solutions (C-C METE nanobeam). (*L* = 80 nm; *h* = 10 nm; Δ*T* = 0; *V*₀ = 0; *P*₀ = 0; *A*₀ = 0; μ = 0; *k*₁ = *k*₂ = *k*₃ = 0.)

Grid Size, <i>N</i>	ω ₁	ω ₂	ω ₃	ω ₄	ω ₅
3	14.5445	145.484	165.349	—	—
5	7.6348	30.1832	44.1502	147.015	161.182
7	7.6440	19.0072	32.8765	74.905	88.464
9	7.6460	18.6790	32.4585	50.130	64.8814
11	7.6460	18.6790	32.4772	48.095	64.0633
13	7.6460	18.6790	32.4765	48.006	64.1910
Exact results [46]	7.6473	18.6692	32.4618	—	—
PDQM [47]	7.6267	18.6229	32.3964	—	—
Computational time	0.15 s	A non-uniform grid with more than 11 nodes			

The Sinc–Discrete Singular–Convolution Differential Quadrature (Sinc-DQ) method was employed in a regular grid with grid sizes ranging from 3 to 15. The numerical results obtained using the Sinc-DQ method converged to the exact solutions [25] for grid sizes greater than or equal to 9, as shown in Table 3. Additionally, the Sinc-DQ method exhibited superior computational efficiency compared to the PDQM method.

Table 3. Normalized frequencies: Sinc-DQ vs. exact and numerical solutions ((C-C) METE nanobeam). ($L = 80 \text{ nm}$; $h = 10 \text{ nm}$; $\Delta T = 0$; $V_0 = 0$; $P_0 = 0$; $A_0 = 0$; $\mu = 0$; $k_1 = k_2 = k_3 = 0$.)

Grid Size, N	ω_1	ω_2	ω_3	ω_4	ω_5
3	19.512	40.542	75.254	—	—
5	16.3278	37.1149	68.3338	152.781	178.53
7	9.5236	25.457	40.2145	60.214	78.254
9	7.6469	18.6977	32.5948	48.1074	64.802
11	7.6469	18.6977	32.5948	48.1074	64.802
Exact results [46]	7.6473	18.6692	32.4618	—	—
PDQM [47]	7.6267	18.6229	32.3964	—	—
Computational time	0.12 s	A uniform grid with more than 9 nodes			

The Discrete Singular Convolution Differential Quadrature Method utilizing the Delta Lagrange Kernel (DSCDQM-DLK) was implemented in a uniform grid with sizes ranging from 3 to 11. The kernel’s bandwidth was adjusted between 3 and 9. As shown in Table 4, the numerical results obtained through the DSCDQM-DLK method converged to the exact solutions [47] when the grid sizes and bandwidths were 3 or greater. Tables 4 and 5 indicate that the DSCDQM-DLK method demonstrated greater computational efficiency compared to both the PDQM and the Sinc-DQ method.

Table 4. Fundamental frequency convergence: DSCDQM-DLK ((C-C) METE nanobeam). ($L = 80 \text{ nm}$; $h = 10 \text{ nm}$; $\Delta T = 0$; $V_0 = 0$; $P_0 = 0$; $A_0 = 0$; $\mu = 0$; $k_1 = k_2 = k_3 = 0$.)

Fundamental Frequency						
Bandwidth	N	3	5	7	9	11
3	7.6469	7.6469	7.6469	7.6469	7.6469	7.6469
5	7.6469	7.6469	7.6469	7.6469	7.6469	7.6469
7	7.6469	7.6469	7.6469	7.6469	7.6469	7.6469
9	7.6469	7.6469	7.6469	7.6469	7.6469	7.6469
Computational time	0.09 s	A uniform grid with more than 9 nodes				

Table 5. Normalized frequencies: DSCDQM-DLK vs. exact and numerical solutions ((C-C) METE nanobeam). ($L = 80 \text{ nm}$; $h = 10 \text{ nm}$; $\Delta T = 0$; $V_0 = 0$; $P_0 = 0$; $A_0 = 0$; $\mu = 0$; $k_1 = k_2 = k_3 = 0$.)

N	1	2	3	4	5
3	7.6469	18.6977	32.5948	48.1074	64.802
5	7.6469	18.6977	32.5948	48.1074	64.802
7	7.6469	18.6977	32.5948	48.1074	64.802
9	7.6469	18.6977	32.5948	48.1074	64.802
Exact results [46]	7.6473	18.6692	32.4618	—	—
PDQM [47]	7.6267	18.6229	32.3964	—	—
Computational time	0.09 s	A uniform grid with more than 3 nodes			

A uniform grid with three to nine nodes was used to develop the Discrete Singular Convolution Differential Quadrature Method utilizing the Regularized Shannon Kernel (DSCDQM-RSK). The kernel bandwidth (3–7) and $\sigma (h_x \text{ to } 1.75 h_x)$, where $h_x = 1/(N-1)$, were varied. Table 6 explains the convergence to the exact solutions [46,47] for grid sizes, bandwidths, and regularization parameters that exceeded specific thresholds. Table 7 highlights the superior computational efficiency among the methods compared.

Table 6. Normalized fundamental frequency convergence (DSCDQM-RSK, (C-C) METE nanobeam). ($L = 80 \text{ nm}$; $h = 10 \text{ nm}$; $\Delta T = 0$; $V_0 = 0$; $P_0 = 0$; $A_0 = 0$; $\mu = 0$; $k_1 = k_2 = k_3 = 0$.)

N	2M + 1	$\sigma = 0.5 h_x$	$\sigma = h_x$	$\sigma = 1.25 h_x$	$\sigma = 1.5 h_x$	$\sigma = 1.75 h_x$
3	3	9.5336	8.7325	8.3112	7.9568	7.6469
	5	9.5336	8.7325	8.3112	7.9568	7.6469
	7	9.5336	8.7325	8.3112	7.9568	7.6469
5	3	9.5336	8.7325	8.3112	7.9568	7.6469
	5	9.5336	8.7325	8.3112	7.9568	7.6469
	7	9.5336	8.7325	8.3112	7.9568	7.6469
7	3	9.5336	8.7325	8.3112	7.9568	7.6469
	5	9.5336	8.7325	8.3112	7.9568	7.6469
	7	9.5336	8.7325	8.3112	7.9568	7.6469
9	3	9.5336	8.7325	8.3112	7.9568	7.6469
	5	9.5336	8.7325	8.3112	7.9568	7.6469
	7	9.5336	8.7325	8.3112	7.9568	7.6469

Table 7. Normalized frequencies of (C-C) METE nanobeam using DSCDQM-RSK. ($L = 80 \text{ nm}$; $h = 10 \text{ nm}$; $\Delta T = 0$; $V_0 = 0$; $P_0 = 0$; $A_0 = 0$; $\mu = 0$; $k_1 = k_2 = k_3 = 0$.)

Grid Size, N	ω_1	ω_2	ω_3	ω_4	ω_5
3	7.6469	18.6977	32.5948	48.1074	64.802
5	7.6469	18.6977	32.5948	48.1074	64.802
7	7.6469	18.6977	32.5948	48.1074	64.802
9	7.6469	18.6977	32.5948	48.1074	64.802
Exact results [46]	7.6473	18.6692	32.4618	—	—
PDQM [47]	7.6267	18.6229	32.3964	—	—
Computational time	0.053	A uniform grid with more than 3 nodes			

This research investigated the influence of various factors on the vibrational behavior of a nanobeam. Using the DSCDQM-RSK method (grid size, 3; bandwidth, 7; $\sigma = 1.75 h_x$), a parametric study examined the effects of linear (and nonlinear) elastic foundation parameters, temperature, electric voltage, nonlocality, the aspect ratio, axial force, magnetic potential, and different boundary conditions (clamped–clamped, clamped–simply supported, simply supported–simply supported) on natural frequencies and mode shapes. The results (Tables 8–11) show that increased linear foundation parameters and magnetic potential raised the fundamental frequency, while the nonlinear foundation parameter had a negligible effect.

The fundamental frequency of the nanobeam was inversely related to the temperature change, electric voltage, non-local parameter, and length-to-thickness ratio (Figures 2–6) but directly related to the axial force and magnetic potential (Figures 7–11). Figures 5, 6, 10 and 11 show the first three modes (transverse displacement and electric potential), revealing that increasing linear (and nonlinear) elastic foundation parameters amplified both displacement and electric potential amplitudes.

The nanobeam’s response was more strongly influenced by the axial force and electric and magnetic fields than by temperature variations. Comparisons between $\text{BiTiO}_3\text{-COFe}_2\text{O}_4$ and $\text{PTZ-5H-COFe}_2\text{O}_4$ show that the former consistently exhibited a higher fundamental frequency, amplitude, and electric potential. The numerical results, accurate and convergent with other methods, offer valuable design insights for creating customized nanoelectronic and biotechnological smart nanostructures.

Table 8. Axial force vs. normalized frequency ((C-C) METE nanobeam). ($L = 60 \text{ nm}$; $h = 10 \text{ nm}$; $\Delta T = 0$; $V_0 = 0$; $A_0 = 0$; $\mu = 0.1$.)

Axial Forces		$P_0 = -1.5$		$P_0 = -1$		$P_0 = 0$		$P_0 = 1$	
Frequencies		ω_1	ω_2	ω_1	ω_2	ω_1	ω_2	ω_1	ω_2
Elastic Parameter									
$k_3 = k_2$	k_1								
0	0	11.745	24.203	11.781	24.264	11.85	24.383	11.919	24.502
	5	11.749	24.2055	11.784	24.266	11.854	24.385	11.923	24.504
	10	11.753	24.207	11.788	24.267	11.858	24.387	11.927	24.506
	15	11.757	24.2091	11.792	24.269	11.862	24.389	11.931	24.507
	25	11.765	24.213	11.8	24.273	11.869	24.392	11.938	24.511
0.025	0	11.752	24.2147	11.787	24.275	11.857	24.394	11.926	24.513
	5	11.756	24.5165	11.791	24.277	11.861	24.396	11.93	24.515
	10	11.76	24.2184	11.795	24.278	11.865	24.398	11.934	24.517
	15	11.764	24.22	11.799	24.28	11.868	24.4	11.937	24.518
	25	11.772	24.224	11.807	24.284	11.876	24.403	11.945	24.522
0.05	0	11.76	24.226	11.794	24.286	11.864	24.405	11.933	24.524
	5	11.763	24.2276	11.798	24.288	11.867	24.407	11.936	24.526
	10	11.767	24.229	11.802	24.289	11.871	24.409	11.94	24.527
	15	11.771	24.231	11.806	24.291	11.875	24.411	11.944	24.529
	25	11.778	24.235	11.813	24.295	11.883	24.414	11.952	24.533
0.1	0	11.772	24.248	11.807	24.308	11.877	24.427	11.946	24.546
	5	11.776	24.25	11.811	24.31	11.881	24.429	11.95	24.547
	10	11.78	24.252	11.815	24.312	11.884	24.431	11.953	24.549
	15	11.784	24.253	11.819	24.313	11.888	24.433	11.957	24.551
	25	11.792	24.257	11.827	24.317	11.896	24.436	11.965	24.555
0.15	0	11.786	24.27	11.821	24.33	11.89	24.449	11.959	24.567
	5	11.79	24.272	11.825	24.332	11.894	24.451	11.963	24.569
	10	11.793	24.274	11.828	24.334	11.898	24.453	11.966	24.571
	15	11.797	24.276	11.832	24.335	11.902	24.454	11.97	24.573
	25	11.81	24.279	11.84	24.339	11.909	24.458	11.978	24.576

Table 9. Magnetic potential vs. normalized frequency ((C-C) METE nanobeam). ($L = 60 \text{ nm}$; $h = 10 \text{ nm}$; $\Delta T = 0$; $V_0 = 0$; $P_0 = 0$; $\mu = 0.1$.)

Magnetic Potential		$A_0 = -0.02$		$A_0 = -0.01$		$A_0 = 0$		$A_0 = 0.01$	
Frequencies		ω_1	ω_2	ω_1	ω_2	ω_1	ω_2	ω_1	ω_2
Elastic Parameter									
$k_3 = k_2$	k_1								
0	0	11.599	23.953	11.726	24.169	11.85	24.383	11.973	24.595
	5	11.603	23.955	11.73	24.171	11.854	24.385	11.977	24.597
	10	11.607	23.957	11.733	24.173	11.858	24.387	11.981	24.598
	15	11.611	23.959	11.737	24.175	11.862	24.389	11.985	24.60
	25	11.619	23.963	11.745	24.179	11.869	24.392	11.992	24.604
0.025	0	11.606	23.965	11.732	24.181	11.857	24.394	11.98	24.606
	5	11.61	23.967	11.736	24.182	11.861	24.396	11.984	24.607
	10	11.614	23.968	11.74	24.184	11.865	24.398	11.987	24.609
	15	11.618	23.97	11.744	24.186	11.868	24.4	11.991	24.611
	25	11.626	23.974	11.752	24.19	11.876	24.403	11.999	24.615
0.05	0	11.613	23.976	11.739	24.192	11.864	24.405	11.986	24.616
	5	11.617	23.978	11.743	24.193	11.867	24.407	11.99	24.618
	10	11.621	23.98	11.747	24.195	11.871	24.409	11.994	24.62
	15	11.625	23.981	11.751	24.197	11.875	24.411	11.998	24.622
	25	11.632	23.985	11.758	24.201	11.883	24.414	12.005	24.625

Table 9. Cont.

Magnetic Potential		$A_0 = -0.02$		$A_0 = -0.01$		$A_0 = 0$		$A_0 = 0.01$	
Frequencies		ω_1	ω_2	ω_1	ω_2	ω_1	ω_2	ω_1	ω_2
Elastic Parameter									
$k_3 = k_2$	k_1								
0.1	0	11.626	23.998	11.752	24.214	11.877	24.427	12	24.638
	5	11.630	24.00	11.756	24.516	11.881	24.429	12.003	24.64
	10	11.634	24.002	11.76	24.217	11.884	24.431	12.007	24.642
	15	11.638	24.004	11.764	24.219	11.888	24.432	12.011	24.644
	25	11.646	24.007	11.772	24.223	11.896	24.436	12.018	24.647
0.15	0	11.64	24.021	11.766	24.236	11.89	24.449	12.013	24.66
	5	11.644	24.022	11.77	24.238	11.894	24.451	12.016	24.662
	10	11.648	24.024	11.774	24.24	11.898	24.453	12.02	24.663
	15	11.652	24.026	11.777	24.241	11.901	24.454	12.024	24.665
	25	11.66	24.03	11.785	24.245	11.909	24.458	12.031	24.669

Table 10. Conditions of boundaries and nonlocal parameter vs. normalized frequency (METE nanobeam). ($L = 80$ nm; $h = 10$ nm; $\Delta T = 0$; $V_0 = 0$; $P_0 = 0$; $A_0 = 0.02$; $\mu = 0$; $L/h = 8$; $k_1 = 10$; $k_2 = 0.25$; $k_3 = 0.15$.)

Normalized Frequencies						
B.C	μ	ω_1	ω_2	ω_3	ω_4	ω_5
CH	0	5.8127	16.5508	30.5288	46.4423	63.1618
	0.05	5.7455	15.8011	27.6732	39.4747	49.9575
	0.1	5.5596	14.0742	22.4378	29.383	34.673
	0.15	5.2935	12.2016	18.0756	22.5677	25.8567
	0.2	4.9905	10.5937	14.9913	18.2813	20.6293
	0.3	4.3971	8.3366	11.3117	13.4537	14.6772
CC	0	7.8228	18.9123	32.7410	48.2897	64.5063
	0.05	7.7286	18.0251	29.6487	41.0333	51.045
	0.1	7.4687	15.9906	24.0051	30.5441	35.4677
	0.15	7.0987	13.8005	19.3378	23.4804	26.4795
	0.2	6.6802	11.9355	16.0648	19.0330	21.0858
	0.3	5.8704	9.3446	12.2038	13.922	14.8882
HH	0	4.0711	14.1202	28.1803	44.4842	61.727
	0.05	4.0296	13.5050	25.2715	37.814	48.785
	0.1	3.9141	12.0759	20.7633	28.1311	33.799
	0.15	3.7468	10.506	16.7268	21.5699	25.1501
	0.2	3.5532	9.1397	13.8537	17.4392	20.0658

Table 11. Comparing the L/t ratio, boundary conditions, and normalized frequencies for METE nanobeams. ($\Delta T = 0$; $V_0 = 0$; $P_0 = 0$; $A_0 = 0.02$; $h = 2$ nm; $\mu = 0$; $k_1 = 10$; $k_2 = 0.25$; $k_3 = 0.15$.)

Normalized Frequencies						
B.C	L/h	ω_1	ω_2	ω_3	ω_4	ω_5
CH	6	65.3075	132.3290	193.2852	240.0726	274.7364
	8	41.9400	87.6475	130.6966	166.538	193.0549
	12	22.8307	48.2839	73.7153	96.2304	114.8452
	16	15.396	32.2589	49.1744	65.2192	78.5352
	20	11.8894	24.2939	37.0331	48.9753	59.8226
	30	8.1887	16.0752	24.0178	31.6047	38.7174

Table 11. Cont.

Normalized Frequencies						
B.C	L/h	ω_1	ω_2	ω_3	ω_4	ω_5
CC	6	51.369	120.3003	184.3095	234.5509	271.6168
	8	32.9497	78.0707	122.6264	160.4316	189.2995
	12	18.3886	42.4297	67.8774	91.1052	110.9483
	16	12.6912	28.4750	44.9936	61.2217	75.2852
	20	10.1075	21.495	33.8316	45.7028	56.9546
	30	7.244	14.4196	22.0180	29.4070	36.6993
HH	6	39.045	107.2164	174.6817	228.4481	268.5102
	8	25.4156	68.2893	114.1099	153.9207	185.1885
	12	14.8655	36.8893	62.0062	85.8467	106.6789
	16	10.7651	24.8817	41.0727	57.1300	71.8685
	20	8.6841	19.0506	30.7592	42.589	53.8329
	30	6.8041	13.008	20.1487	27.4042	34.5047

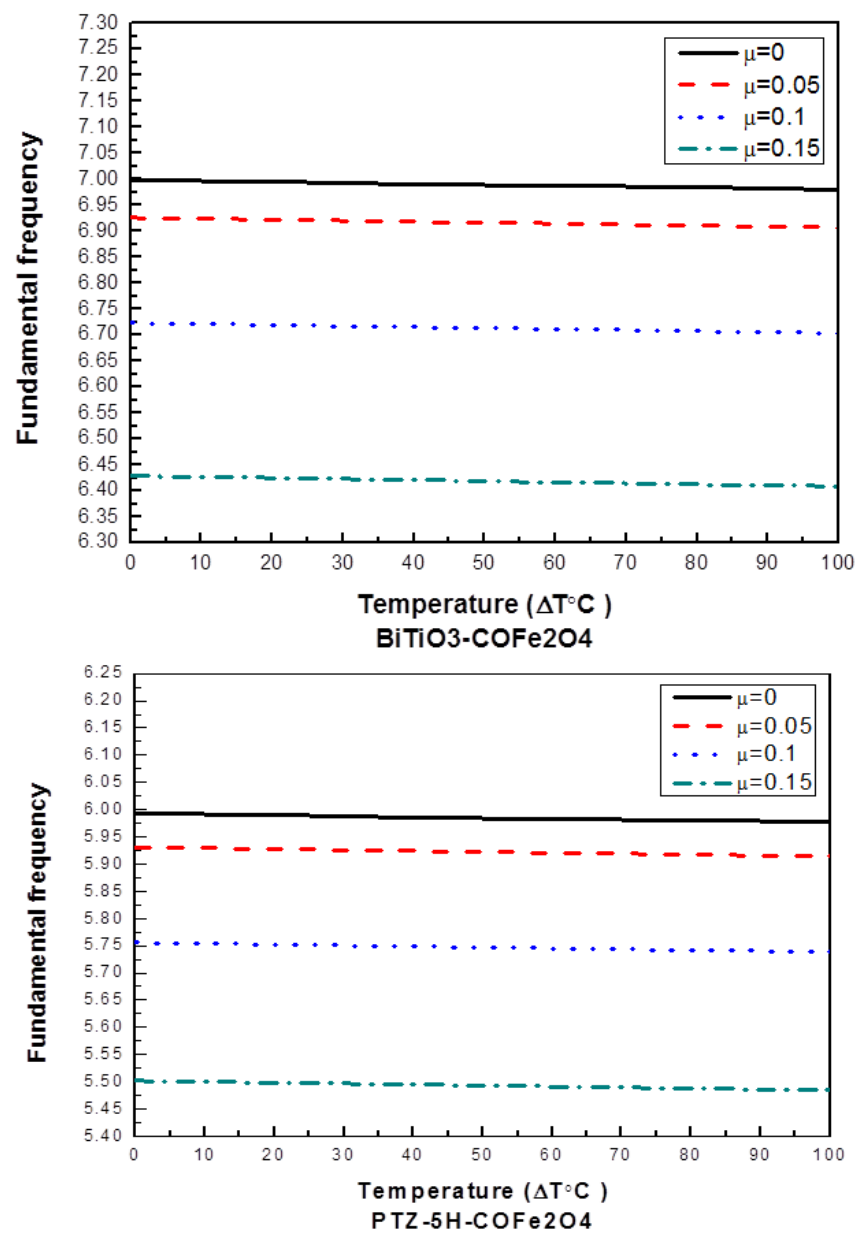


Figure 2. Impact of temperature and nonlocal parameter on fundamental frequency of hinged-hinged (H-H) METE nanobeam for different materials. $V_0 = 0$; $P_0 = 1.5$; $A_0 = 0.02$; $h = 10$ nm; $L/h = 6$; $k_1 = 25$; $k_2 = 0.05$; $k_3 = 0.15$.

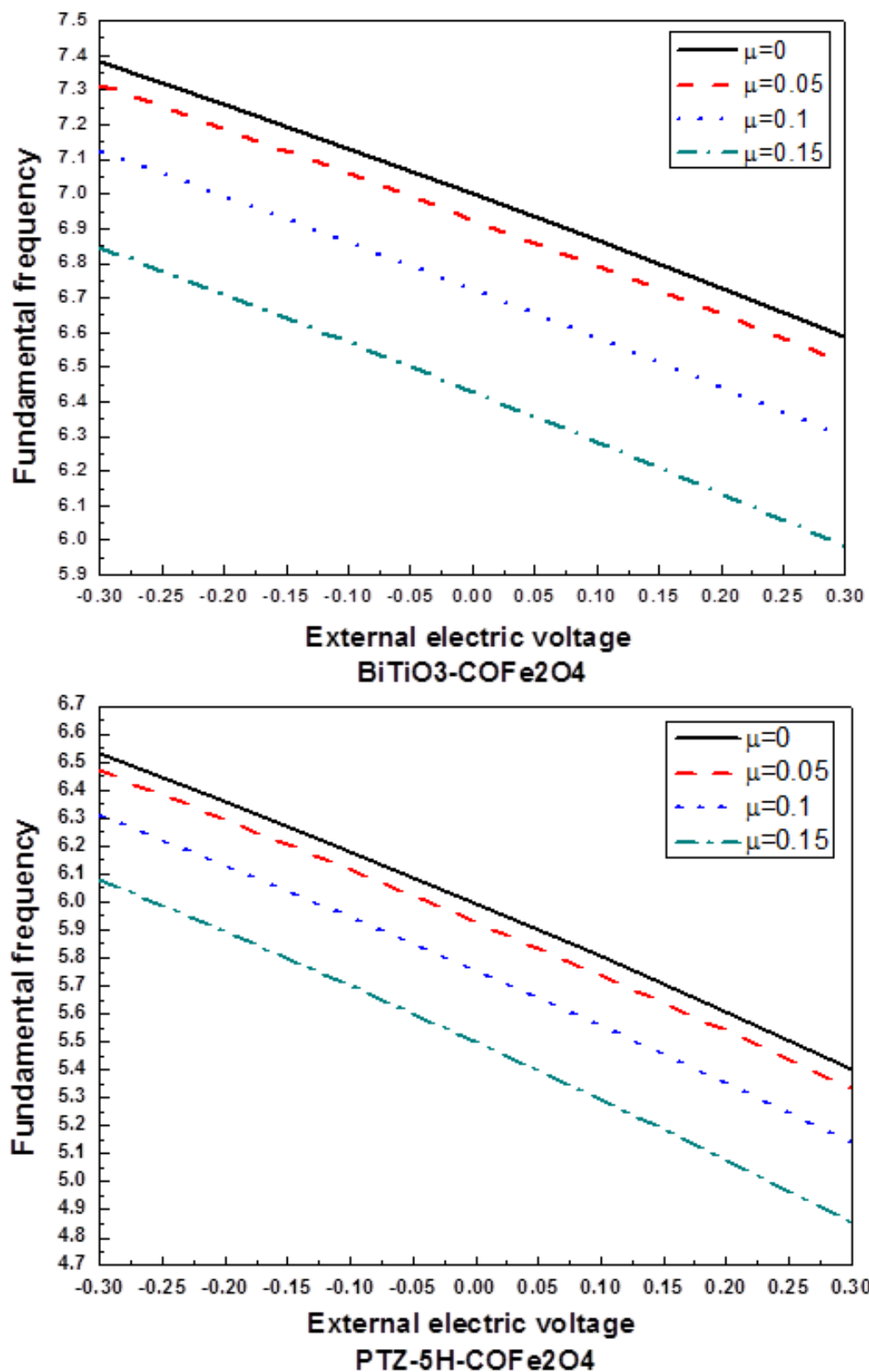


Figure 3. Impact of electric voltage and nonlocal parameter on fundamental frequency of (H-H) METE nanobeam for different materials. $\Delta T = 0$; $P_0 = 1.5$; $A_0 = 0.02$; $h = 10$ nm; $L/h = 6$; $k_1 = 25$; $k_2 = 0.05$; $k_3 = 0.15$.

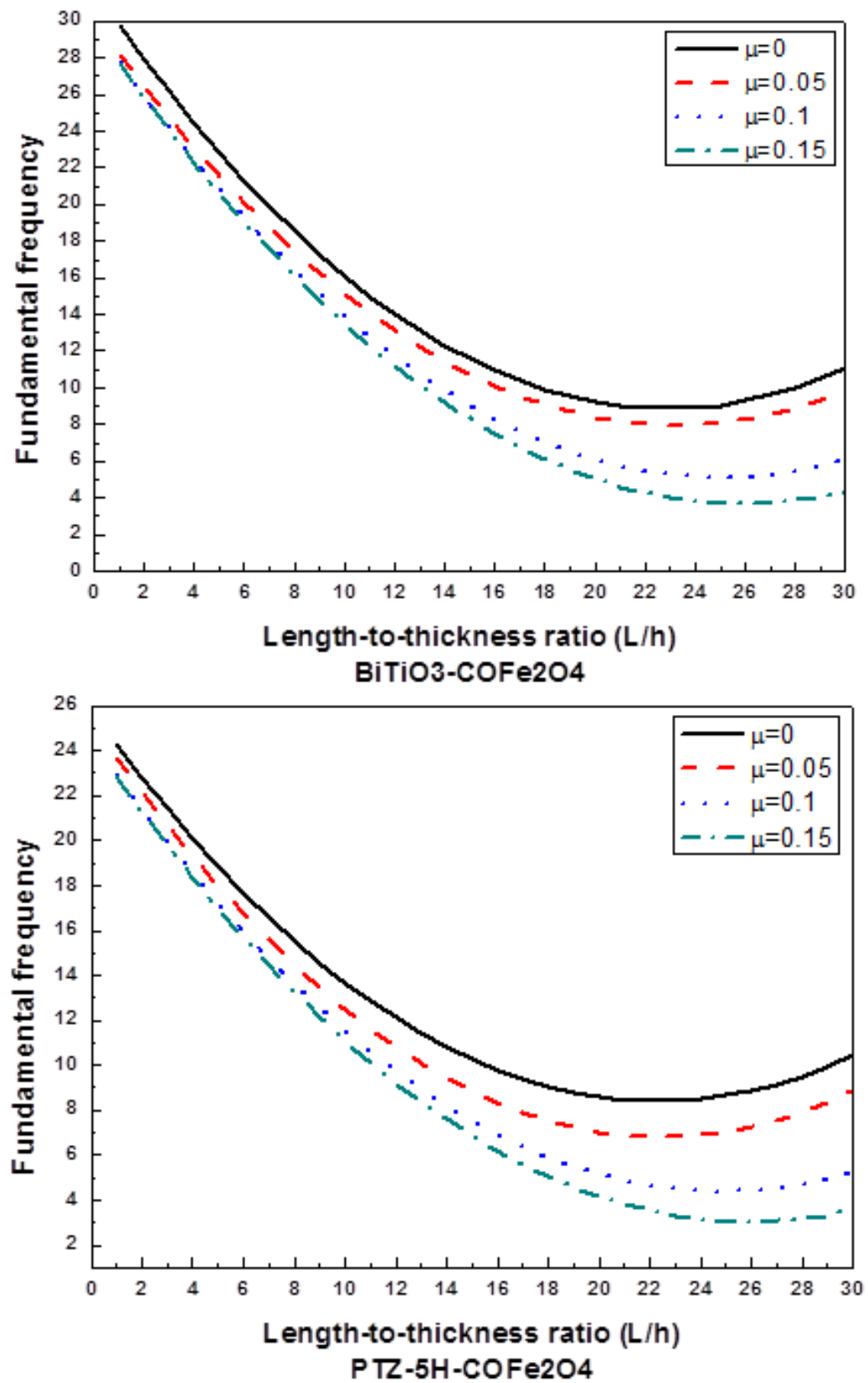


Figure 4. Impact of length-to-thickness ratio and nonlocal parameter on fundamental frequency of (H-H) METE nanobeam for different materials. $P_0 = 2$; $\Delta T = 100$; $V_0 = -0.3$; $A_0 = 0.02$; $h = 2$ nm; $k_1 = 25$; $k_2 = 0.05$; $k_3 = 0.15$.

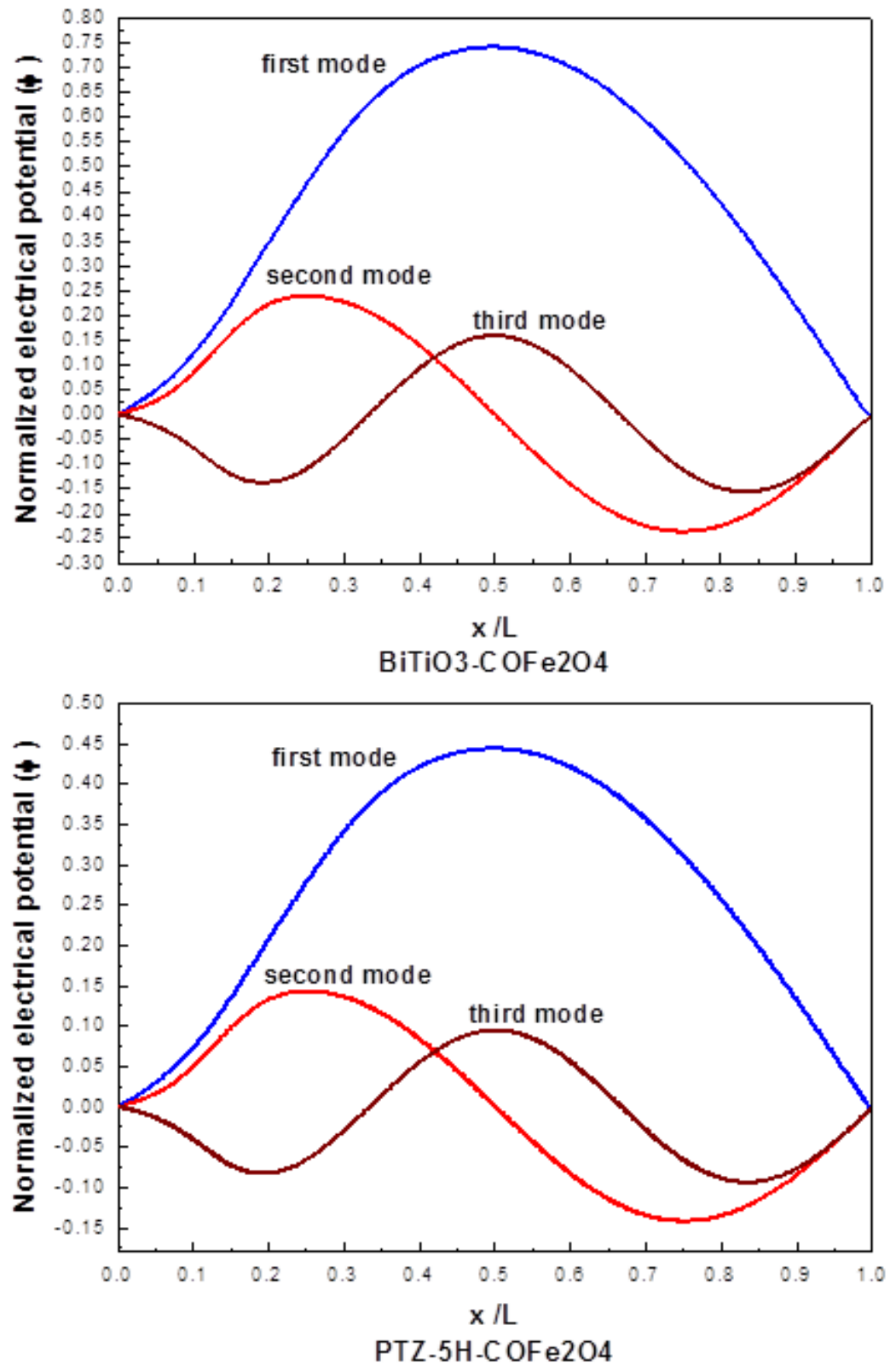


Figure 5. Electrical potential distribution in (C-C) METE nanobeam for different materials. $P_0 = 0$; $\Delta T = 100$; $V_0 = -0.3$; $A_0 = 0.05$; $h = 10$ nm; $L/h = 6$; $k_1 = k_2 = k_3 = 0$.

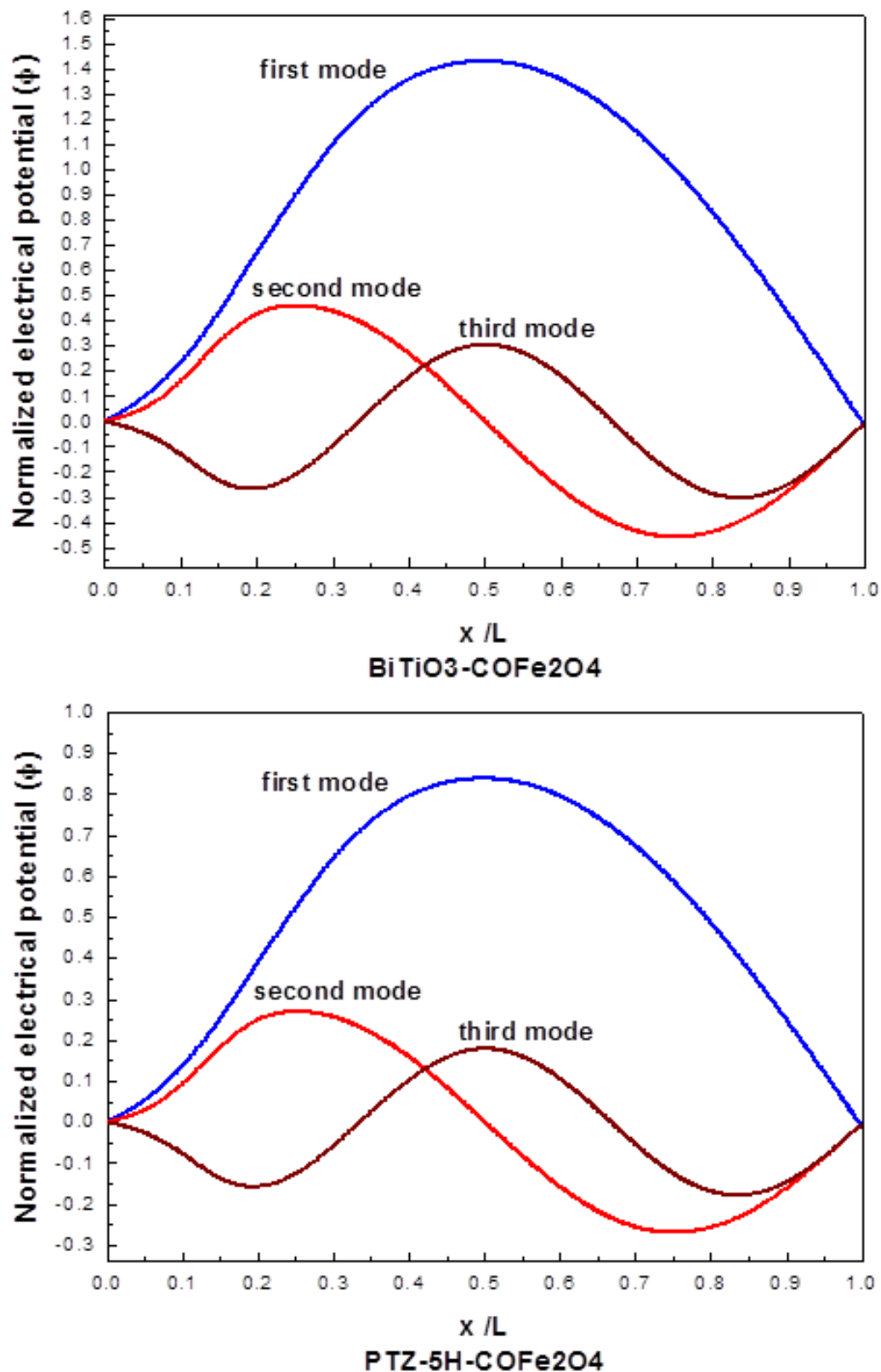


Figure 6. Electrical potential distribution in (C-C) METE nanobeam for different materials. $P_0 = 0$; $\Delta T = 100$; $V_0 = -0.3$; $A_0 = 0.05$; $h = 10$ nm; $L/h = 6$; $k_1 = 25$; $k_2 = 0.05$; $k_3 = 0.15$.

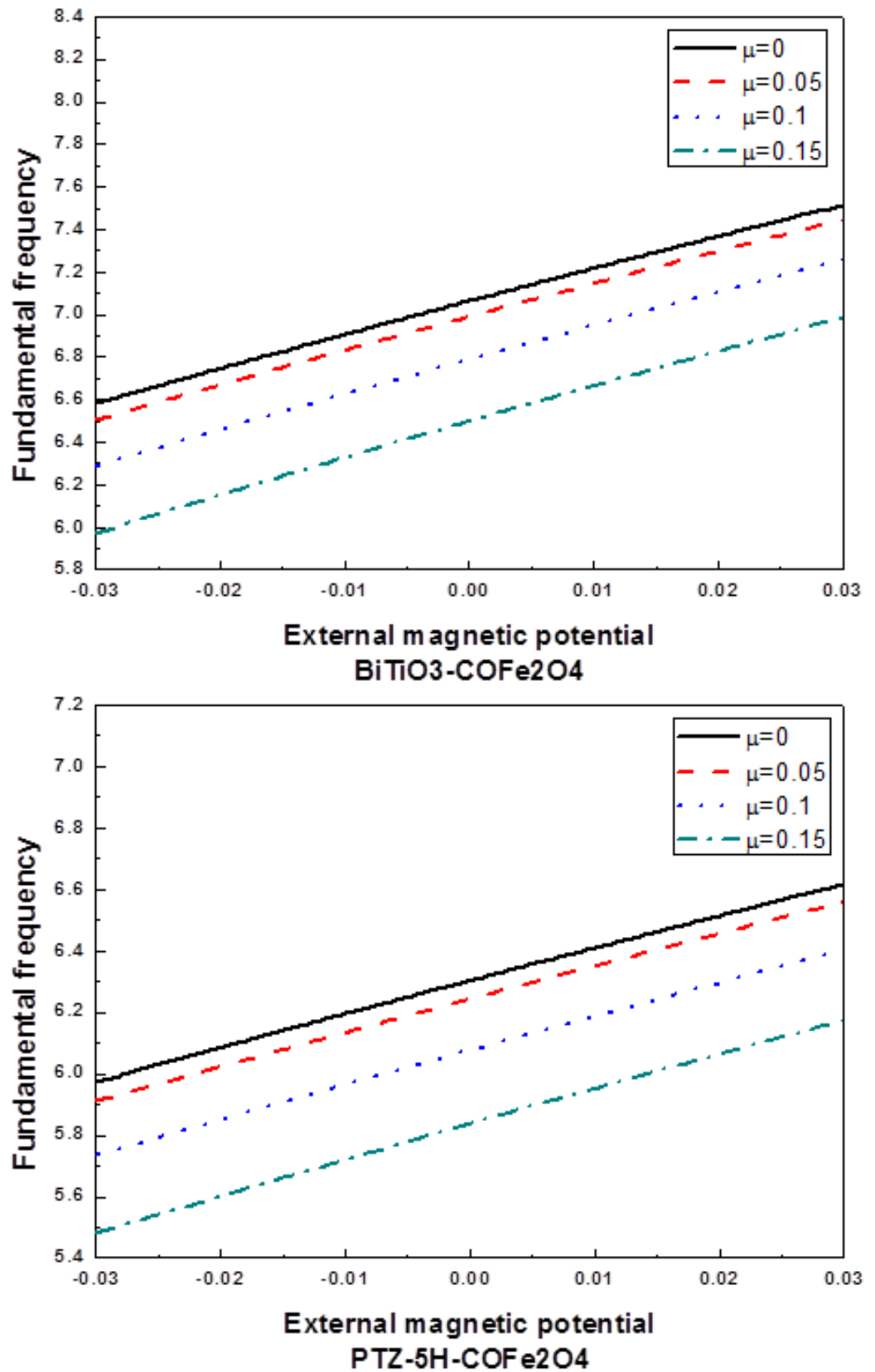


Figure 7. Impact of magnetic potential and nonlocal parameter on fundamental frequency of (H-H) METE nanobeam for different materials. $\Delta T = 100$; $P_0 = 1.5$; $A_0 = 0.02$; $h = 10$ nm; $L/h = 6$; $k_1 = 25$; $k_2 = 0.05$; $k_3 = 0.15$.

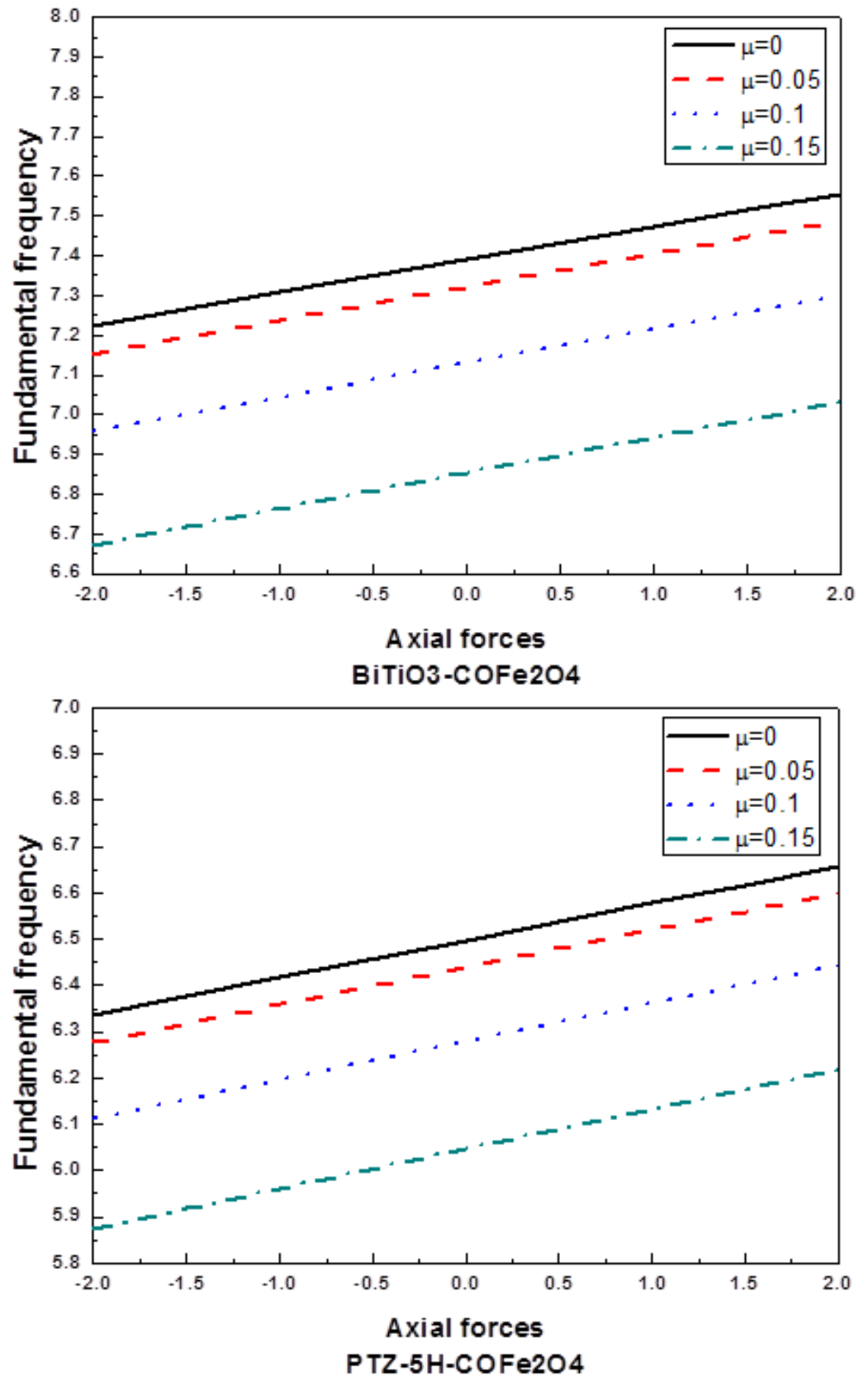


Figure 8. Impact of axial force and nonlocal parameter on fundamental frequency of (H-H) METE nanobeam for different materials. $\Delta T = 100$; $V_0 = -0.3$; $A_0 = 0.03$; $h = 10$ nm; $L/h = 6$; $k_1 = 25$; $k_2 = 0.05$; $k_3 = 0.15$.

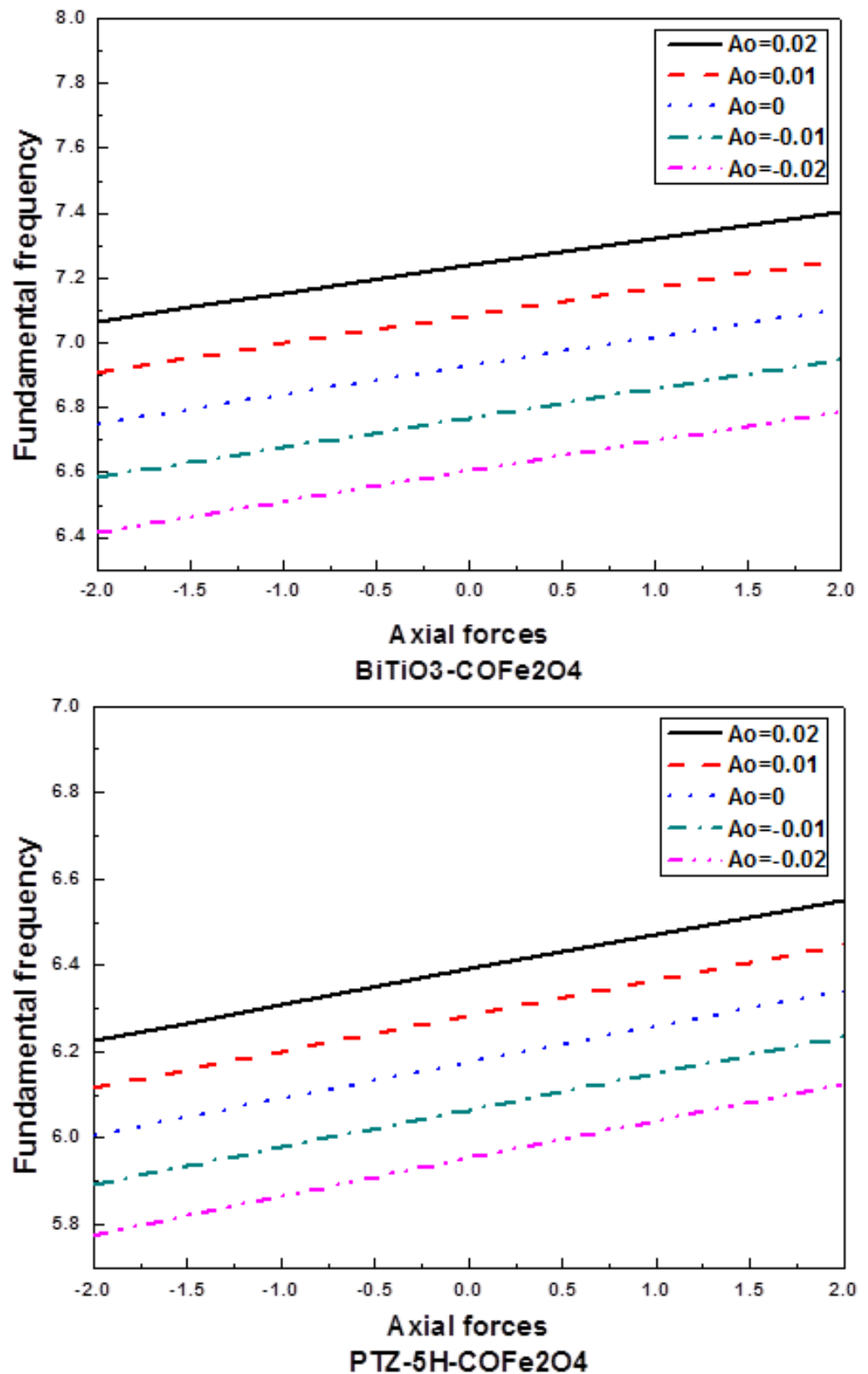


Figure 9. Impact of axial force and magnetic potential on fundamental frequency of (H-H) METE nanobeam for different materials. $\Delta T = 100$; $V_0 = -0.3$; $\mu = 0.01$; $h = 10$ nm; $L/h = 6$; $k_1 = 25$; $k_2 = 0.05$; $k_3 = 0.15$.

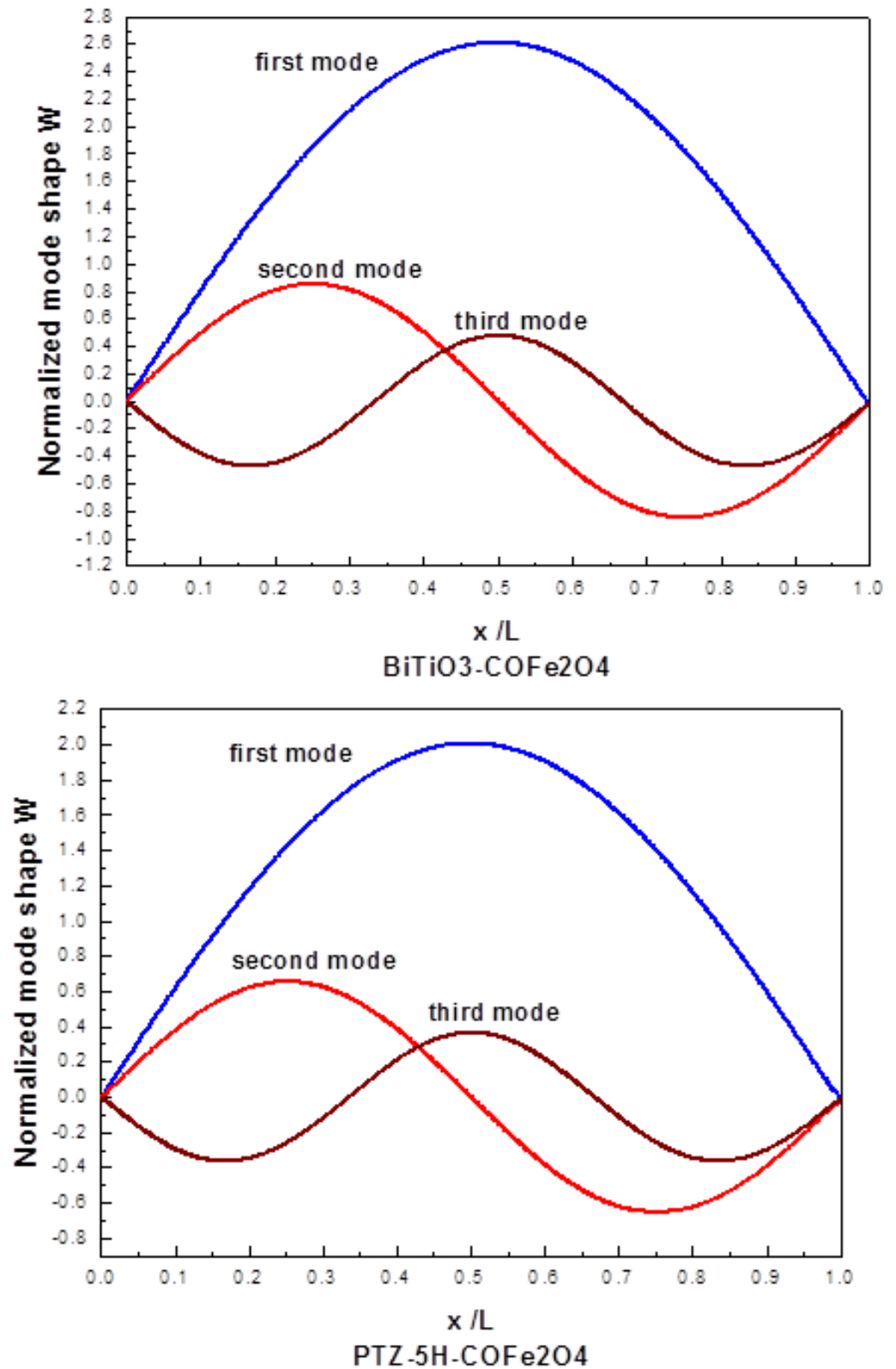


Figure 10. Mode shapes of (H-H) METE nanobeam for different materials. $P_0 = 0$; $\Delta T = 100$; $V_0 = -0.3$; $A_0 = 0.05$; $h = 10$ nm; $L/h = 6$; $k_1 = k_2 = k_3 = 0$.

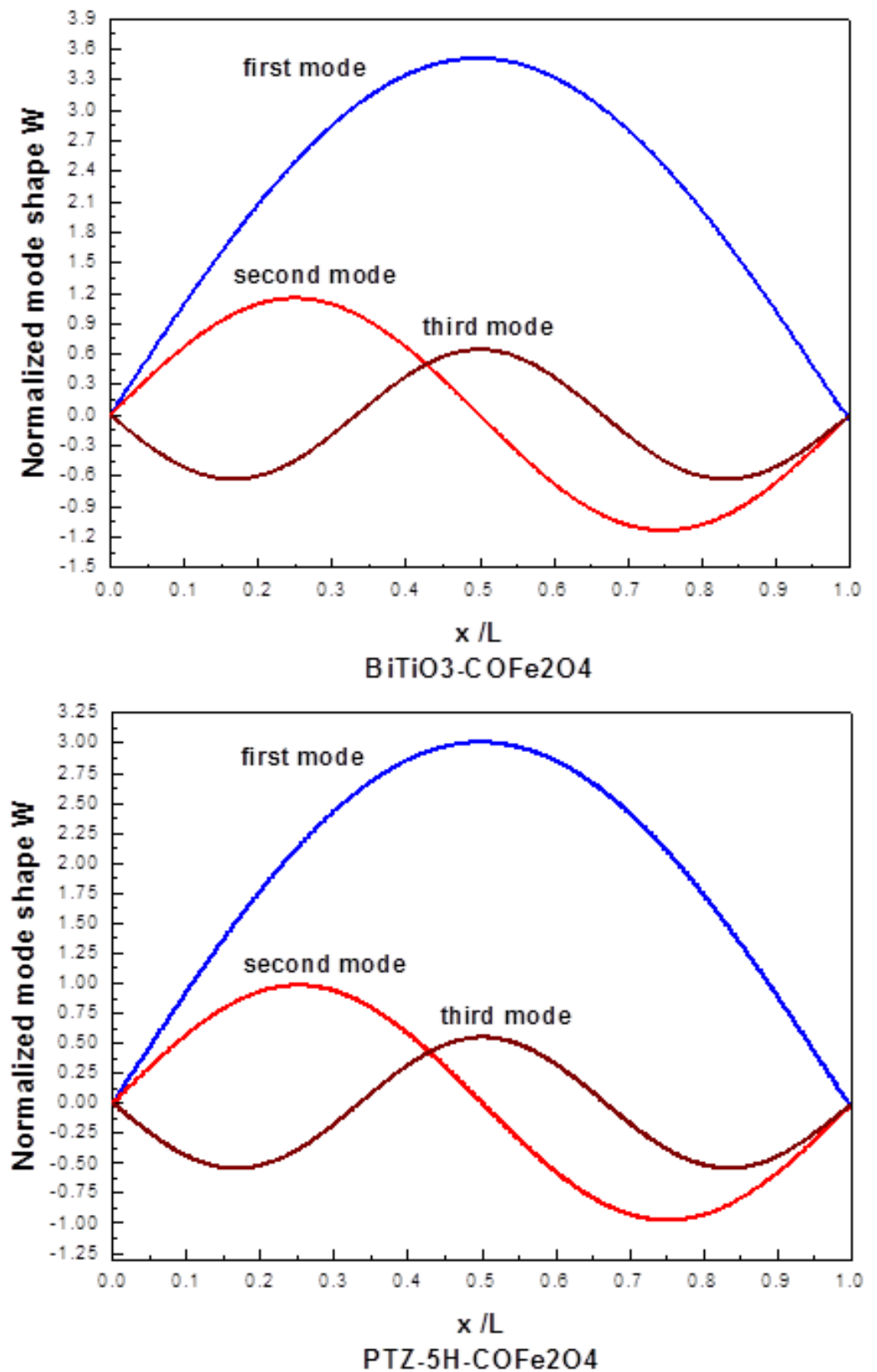


Figure 11. Mode shapes of (H-H) METE nanobeam for different materials. $P_0 = 0$; $\Delta T = 100$; $V_0 = -0.3$; $A_0 = 0.05$; $h = 10$ nm; $L/h = 6$; $k_1 = 25$; $k_2 = 0.05$; $k_3 = 0.15$.

5. Discussion

In this section, we introduce the potential advantages and limitations of Ritz methods compared to the DQMs employed in this study: Ritz methods, such as those employing Ritz power series interpolation, often involve simpler discretization procedures compared to DQMs. They typically require fewer grid points, which can lead to reduced computational cost, especially for problems with simple geometries. The use of analytical basis functions, such as polynomials, can provide insights into the analytical behavior of the system and facilitate the understanding of the underlying physics. However, Ritz methods can be challenging to apply to problems with complex geometries or boundary conditions. The convergence of the Ritz method can be sensitive to the choice of basis functions and the number of terms included in the series. Implementing complex material properties, such as those encountered in METE materials, within the Ritz framework can be more intricate than in DQMs. DQMs are highly versatile and can be applied to problems with complex geometries, boundary conditions, and material properties. DQMs can achieve high accuracy with relatively few grid points, making them computationally efficient for many problems. DQMs can be easily adapted to different types of differential equations and boundary conditions. However, the accuracy and convergence of DQM solutions can be sensitive to the choice of grid point distribution. In some cases, DQMs can exhibit numerical instability, particularly for higher-order derivatives. While Ritz methods offer a simpler discretization process, DQMs demonstrate greater versatility and adaptability for handling complex problems encountered in the analysis of METE nanostructures. The choice of the most suitable method depends on the specific characteristics of the problem under consideration, including geometry, boundary conditions, material properties, and computational resources. This brief comparison provides a broader perspective for future readers and encourages the further exploration of alternative numerical techniques for analyzing the dynamics of METE nanostructures.

6. Conclusions

This research provides a highly accurate numerical analysis (error $< 10^{-10}$) of the vibrational behavior of METE nanobeams, employing three distinct differential quadrature methods (PDQM, Sinc-DQ, and DSCDQM-RSK) implemented via a custom MATLAB program. A parametric study investigated how various factors influence nanobeam vibration, revealing key insights into their behavior:

- The fundamental frequency increased with increasing axial forces, external magnetic potential, and linear elastic foundation characteristics.
- On the other hand, the fundamental frequency decreased when the temperature and the length-to-thickness ratio, nonlocal factors, and external electric voltage increased.
- Increased displacement and electrical potential amplitudes were associated with higher linear (and nonlinear) elastic foundation parameters.
- BiTiO₃-COFe₂O₄ outperformed PTZ-5H-COFe₂O₄, exhibiting higher fundamental frequency and greater normalized amplitude and electrical potential.

The numerical methods presented accurately and efficiently analyze the dynamic behavior of METE nanobeams. These results are significant for designing and optimizing smart nanostructures with customized properties for nanoelectronics and biotechnology.

Funding: This research received no external funding.

Data Availability Statement: The data presented in this study are available in the article.

Conflicts of Interest: The authors declare no conflicts of interest.

References

1. Jandaghian, A.; Jafari, A.; Rahmani, O. Exact solution for Transient bending of a circular plate integrated with piezoelectric layers. *Appl. Math. Model.* **2013**, *37*, 7154–7163. <http://doi.org/10.1016/j.apm.2013.02.007>.
2. Nan, C.W. Magneto electric effect in composites of piezoelectric and piezomagnetic phases. *Phys. Rev. B* **1994**, *50*, 6082–6088. <https://doi.org/10.1103/PhysRevB.50.6082>.
3. Zhai, J.; Xing, Z.; Dong, S.; Li, J.; Viehland, D. Magnetolectric laminate composites: An overview. *J. Am. Ceram. Soc.* **2008**, *91*, 351–358. <https://doi.org/10.1111/j.1551-2916.2008.02259.x>
4. Nan, C.W.; Bichurin, M.; Dong, S.; Viehland, D.; Srinivasan, G. Multiferroic magnetolectric composites: Historical perspective, status, and future directions. *J. Appl. Phys.* **2008**, *103*, 031101. <https://doi.org/10.1063/1.2836410>.
5. Wu, C.P.; Tsai, Y.H. Static behavior of functionally graded magneto-electro-elastic shells under electric displacement and magnetic flux. *Int. J. Eng. Sci.* **2007**, *45*, 744–769. <https://doi.org/10.1016/j.ijengsci.2007.05.002>.
6. Huang, D.J.; Ding, H.J.; Chen, W.Q. Static analysis of anisotropic functionally graded magneto-electro-elastic beams subjected to arbitrary loading. *Eur. J. Mech.* **2010**, *29*, 356–369. <https://doi.org/10.1016/j.euromechsol.2009.12.002>.
7. Chang, T.P. Deterministic and random vibration analysis of fluid-contacting transversely isotropic magneto-electro-elastic plates. *Comput. Fluids* **2013**, *84*, 247–254. <https://doi.org/10.1016/j.compfluid.2013.06.009>.
8. Ansari, R.; Gholami, R.; Rouhi, H. Size-dependent nonlinear forced vibration analysis of magneto-electro-thermo-elastic Timoshenko nanobeams based upon the nonlocal elasticity theory. *Compos. Struct.* **2015**, *126*, 216–226. <https://doi.org/10.1016/j.compstruct.2015.02.068>.
9. Ke, L.L.; Wang, Y.S.; Yang, J.; Kitipornchai, S. The size dependent vibration of embedded magneto-electro-elastic cylindrical nanoshells. *Smart Mater. Struct.* **2014**, *23*, 125036. <https://doi.org/10.1088/0964-1726/23/12/125036>.
10. Prashanthi, K.; Shaibani, P.M.; Sohrabi, A.; Natarajan, T.S.; Thundat, T. Nanoscale magnetolectric coupling in multiferroic BiFeO₃ nanowires. *Phys. Status Solidi R* **2012**, *6*, 244–246. <https://doi.org/10.1002/pssr.201206135>.
11. Martin, L.W.; Crane, S.P.; Chu, Y.H.; Holcomb, M.B.; Gajek, M.; Huijben, M.; Yang, C.H.; Balke, N.; Ramesh, R. Multiferroic and magnetolectrics: Thin films and nanostructures. *J. Phys. Condens. Matter.* **2008**, *20*, 434220. <https://doi.org/10.1088/0953-8984/20/43/434220>.
12. Akgöz, B.; Civalek, O. Buckling analysis of cantilever carbon nanotubes using the strain gradient elasticity and modified couple stress theories. *J. Comput. Theor. Nanosci.* **2011**, *8*, 1821–1827. <https://doi.org/10.1166/jctn.2011.1888>.
13. Li, C. A nonlocal analytical approach for torsion of cylindrical nanostructures and the existence of higher-order stress and geometric boundaries. *Compos. Struct.* **2014**, *118*, 607–621. <https://doi.org/10.1016/j.compstruct.2014.08.008>.
14. Shen, Z.B.; Li, X.F.; Sheng, L.P.; Tang, G.J. Transverse vibration of nanotube-based micro-mass sensor via nonlocal Timoshenko beam theory. *Comput. Mater. Sci.* **2012**, *53*, 340–346. <https://doi.org/10.1016/j.commatsci.2011.09.023>.
15. Li, X.F.; Wang, B.L. Vibrational modes of Timoshenko beams at small scales. *Appl. Phys. Lett.* **2009**, *94*, 101903. <https://doi.org/10.1063/1.3094130>.
16. Huang, Y.; Luo, Q.Z.; Li, X.F. Transverse waves propagating in carbon nanotubes via a higher-order nonlocal beam model. *Compos. Struct.* **2013**, *95*, 328–336. <https://doi.org/10.1016/j.compstruct.2012.07.038>.
17. Shen, J.P.; Li, C. A semi-continuum-based bending analysis for extreme-thin micro/nano-beams and new proposal for nonlocal differential constitution. *Compos. Struct.* **2017**, *172*, 210–220. <https://doi.org/10.1016/j.compstruct.2017.03.070>.
18. Mercan, K.; Civalek, O. DSC method for buckling analysis of boron nitride nanotube (BNNT) surrounded by an elastic matrix. *Compos. Struct.* **2016**, *143*, 300–309. <http://doi.org/10.1016/j.compstruct.2016.02.040>.
19. Şimşek, M.; Yurtcu, H. Analytical solutions for bending and buckling of functionally graded nanobeams based on the nonlocal Timoshenko beam theory. *Compos. Struct.* **2013**, *97*, 378–386. <https://doi.org/10.1016/j.compstruct.2012.10.038>.
20. Arefi, M.; Zenkour, A.M. A simplified shear and normal deformations nonlocal theory for bending of functionally graded piezomagnetic sandwich nanobeams in magneto-thermo-electric environment, *J. Sandw. Struct. Mater.* **2016**, *18*, 624–651. <https://doi.org/10.1177/1099636216652581>.
21. Jian, S.P.; Yan, L.; Jie, Y. A Semi Analytical Method for Nonlinear Vibration of Euler-Bernoulli Beams with General Boundary Conditions. *Math. Probl. Eng.* **2010**, *2010*, 591786. <http://doi.org/10.1155/2010/591786>.
22. Norouzzadeh, A.; Ansari, R. Finite element analysis of nano-scale Timoshenko beams using the integral model of nonlocal elasticity. *Phys E.* **2017**, *88*, 194–200. <https://doi.org/10.1016/j.physe.2017.01.006>.
23. Roque, C.M.C.; Fidalgo, D.S.; Ferreira, A.J.M.; Reddy, J.N. A study of a microstructure-dependent composite laminated Timoshenko beam using a modified couple stress theory and a meshless method. *Compos. Struct.* **2013**, *96*, 5325–537. <https://doi.org/10.1016/j.compstruct.2012.09.011>.
24. Foroughi, H.; Azhari, M. Mechanical buckling and free vibration of thick functionally graded plates resting on elastic foundation using the higher order B-spline finite strip method. *Meccanica* **2014**, *49*, 981–993. <https://doi.org/10.1007/s11012-013-9844-2>.
25. Fakher, M.; Shahrokh, H.H. Bending and free vibration analysis of nanobeams by differential and integral forms of nonlocal strain gradient with Rayleigh–Ritz method. *Mater. Res. Express* **2017**, *4*, 125025. <https://doi.org/10.1088/2053-1591/aa9dd6>.

26. Sizikov, V.; Sidorov, D. Generalized quadrature for solving singular integral equations of Abel type in application to infrared tomography. *Appl. Numer. Math.* **2016**, *106*, 69–78.
27. Ragb, O.; Mohamed, M.; Matbuly, M.S.; Civalek, O. Nonlinear Analysis of Organic Polymer Solar Cells Using Differential Quadrature Technique with Distinct and Unique Shape Function. *CMES-Comput. Model. Eng. Sci.* **2023**, *137*, 8992. <https://doi.org/10.32604/cmcs.2023.028992>.
28. Mohamed, M.; Mabrouk, S.M.; Rashed, A.S. Mathematical investigation of the infection dynamics of COVID-19 using the fractional differential quadrature method. *Computation* **2023**, *10*, 198. <https://doi.org/10.3390/computation11100198>.
29. Ragb, O.; Wazwaz, A.M.; Mohamed, M.; Matbuly, M.S.; Salah, M. Fractional differential quadrature techniques for fractional order Cauchy reaction-diffusion equations. *Math. Methods Appl. Sci.* **2023**, *9*, 10216–10233. <https://doi.org/10.1002/mma.9112>.
30. Mustafa, A.; Ragb, O.; Salah, M.; Salama, R.S.; Mohamed, M. Distinctive Shape Functions of Fractional Differential Quadrature for Solving Two-Dimensional Space Fractional Diffusion Problems. *Fractal Fract.* **2023**, *9*, 668. <https://doi.org/10.3390/fractalfract7090668>.
31. Shojaei, M.F.; Ansari, R. Variational differential quadrature: A technique to simplify numerical analysis of structures. *Appl. Math. Model.* **2017**, *49*, 705–738. <https://doi.org/10.1016/j.apm.2017.02.052>.
32. Tornabene, F.; Fantuzzi, N.; Viola, E.; Carrera, E. Static analysis of doubly-curved anisotropic shells and panels using CUF approach, differential geometry and differential quadrature method. *Compos. Struct.* **2014**, *107*, 675–697. <https://doi.org/10.1016/j.compstruct.2013.08.038>.
33. Tornabene, F.; Dimitri, R.; Viola, E. Transient dynamic response of generally shaped arches based on a GDQ-Time-stepping method. *Int. J. Mech. Sci.* **2016**, *114*, 277–314. <https://doi.org/10.1016/j.ijmecsci.2016.05.005>.
34. Korkmaz, A.; İdris, D. Shock wave simulations using Sinc Differential Quadrature Method. *Eng. Comput. Int. J. Comput. Aided Eng. Softw.* **2011**, *28*, 654–674. <https://doi.org/10.1108/02644401111154619>.
35. Ke, L.L.; Wang, Y.S.; Wang, Z.D. Nonlinear vibration of the piezoelectric nanobeams based on the nonlocal theory. *Compos. Struct.* **2012**, *94*, 2038–2047. <https://doi.org/10.1016/j.compstruct.2012.01.023>.
36. Civalek, O.; Kiracioglu, O. Free vibration analysis of Timoshenko beams by DSC method. *Int. J. Numer. Meth. Biomed. Engng.* **2010**, *26*, 250–275. <https://doi.org/10.1002/cnm.1279>.
37. Seçkin, A.; Sarıgül, A.S. Free vibration analysis of symmetrically laminated thin composite plates by using discrete singular convolution (DSC) approach: Algorithm and verification. *J. Sound Vib.* **2009**, *315*, 197–211. <https://doi.org/10.1016/j.jsv.2008.01.061>.
38. Civalek, O. Free vibration of carbon nanotubes reinforced (CNTR) and functionally graded shells and plates based on FSDT via discrete singular convolution method. *Compos. Part B* **2017**, *111*, 45–59. <https://doi.org/10.1016/j.compositesb.2016.11.030>.
39. Civalek, O. Vibration analysis of conical panels using the method of discrete singular convolution. *Commun Numer. Methods Eng.* **2008**, *24*, 169–181. <https://doi.org/10.1002/cnm.961>.
40. Ragb, O.; Mohamed, M.; Matbuly, M.S.; Civalek, O. Sinc and discrete singular convolution for analysis of three-layer composite of perovskite solar cell. *Int. J. Energy Res.* **2022**, *46*, 4279–4300.
41. Jandaghian, A.A.; Rahmani, O. Free vibration analysis of magneto-electrothermo elastic nanobeams resting on a Pasternak foundation. *Smart Mater. Struct.* **2016**, *25*, 035023. <https://doi.org/10.1088/0964-1726/25/3/035023>.
42. Chang, S. *Differential Quadrature and Its Application in Engineering*; Springer-Verlag London Ltd.: London, UK, 2000. <https://doi.org/10.1007/978-1-4471-0407-0>.
43. Mustafa, A.; Salama, R.S.; Mohamed, M. Semi-Analytical Analysis of Drug Diffusion through a Thin Membrane Using the Differential Quadrature Method. *Mathematics* **2023**, *11*, 2998.
44. Abdelfattah, W.M.; Ragb, O.; Salah, M.; Mohamed, M. A Robust and Versatile Numerical Framework for Modeling Complex Fractional Phenomena: Applications to Riccati and Lorenz Systems. *Fractal Fract.* **2024**, *8*, 647.
45. Shashidhar, S.; Jiang, L.Y. The effective magnetolectric coefficients of polycrystalline multiferroic composites. *Acta Mater.* **2005**, *53*, 4135–4142. <https://doi.org/doi:10.1016/j.actamat.2005.05.014>.
46. Jandaghian, A.A.; Rahmani, O. An analytical Solution for Free Vibration of Piezoelectric nanobeams Based on a Nonlocal Elasticity Theory. *Smart Mater. Struct.* **2016**, *32*, 143–151. <https://doi.org/10.1017/jmech.2015.53>.
47. Ke, L.-L.; Wang, Y.-S. Free vibration of size dependent magneto-electro-elastic nanobeams based on the nonlocal theory. *Phys. E* **2014**, *63*, 52–61. <https://doi.org/10.1016/j.physe.2014.05.002>.

Disclaimer/Publisher’s Note: The statements, opinions and data contained in all publications are solely those of the individual author(s) and contributor(s) and not of MDPI and/or the editor(s). MDPI and/or the editor(s) disclaim responsibility for any injury to people or property resulting from any ideas, methods, instructions or products referred to in the content.